Remote Sensing Applications: Society and Environment 36 (2024) 101290

Contents lists available at ScienceDirect

Remote Sensing Applications: Society and Environment

journal homepage: www.elsevier.com/locate/rsase

Spatiotemporal characterization of the subsidence and change detection in Tehran plain (Iran) using InSAR observations and Landsat 8 satellite imagery

Sasan Babaee [a], Mohammad Amin Khalili [b,*], Rita Chirico [c], Anna Sorrentino [b], Diego Di Martire [b]

[a] Department of Geodesy and Geomatics Engineering, K. N. Toosi University of Technology, Tehran, Iran
[b] Department of Earth, Environmental and Resource Sciences, Federico II University of Naples, Naples, Italy
[c] Department of Geosciences - University of Padua, Padova, Italy

ARTICLE INFO

Keywords:
Spatiotemporal subsidence pattern
Radar interferometry
Sentinel-1A
Tehran plain

ABSTRACT

Urban areas worldwide are increasingly facing challenges related to land subsidence, a phenomenon exacerbated by uncontrolled groundwater extraction and urban expansion. This research focuses on the Tehran plain, Iran's capital city, where significant subsidence has been observed due to uncontrolled migrations influenced by various economic and political factors. This expansion has increased demand for energy, notably water, leading to irregular water withdrawals from underground sources and, consequently, land subsidence. Monitoring this subsidence, particularly its effects on urban infrastructure, has become a critical challenge. This research first reviewed the existing body of knowledge related to subsidence measurement in the Tehran plain with an emphasis on their findings and limitations and then used radar images to study the subsidence patterns in the Tehran plain from 2016 to the end of 2020. Finally, the results collaborated by optical imagery analysis to find the relationship between surface change detection and spatiotemporal distribution of subsidence. As a result, through processing Sentinel-1A SAR images, consistent vertical displacements (subsidence) were observed, especially in areas heavily reliant on groundwater from wells, with some areas experiencing a rate of more than −20 mm/year. Horizontal displacement, however, was approximately about ±8 mm/year. Also, our results show that the subsidence rate in this plain has decreased in recent years. Therefore, the study integrated multispectral satellite data to clarify this issue and compensate for missing groundwater level data, specifically the Normalized-Difference Vegetation Index (NDVI) and Normalized-Difference Moisture Index (NDMI). These datasets were used to monitor changes in vegetation cover distribution and moisture in response to the variations of groundwater depth over time. The results of this research can be beneficial in adequately managing groundwater resource utilization to reduce the potential damage to infrastructure and the environment.

1. Introduction

Land subsidence, a phenomenon where the ground surface sinks relative to a datum, is an increasingly critical issue affecting urban

* Corresponding author. Monte Sant'Angelo Campus 80126, Federico II University of Naples, Naples, Italy.
E-mail address: mohammadamin.khalili@unina.it (M.A. Khalili).

https://doi.org/10.1016/j.rsase.2024.101290
Received 18 November 2023; Received in revised form 21 June 2024; Accepted 4 July 2024
Available online 6 July 2024

areas globally (Aljammaz et al., 2021; Khalili et al., 2023). Driven by factors such as groundwater extraction, natural compaction of sediment, and anthropogenic activities, subsidence can result in significant infrastructural damage, increased flooding risk, and environmental degradation (Santos et al., 2012; Bagheri-Gavkosh et al., 2021; Bausilio et al., 2024). Recent research has highlighted subsidence issues in various parts of the world, including Jakarta, Indonesia, which faces severe subsidence due to excessive groundwater extraction, and Venice, Italy, where both natural and human-induced factors contribute to the sinking city (Park et al., 2016; Tzampoglou et al., 2023). These studies underscore the need for comprehensive monitoring and mitigation strategies to manage subsidence effectively.

Advanced remote sensing technologies, particularly Interferometric Synthetic Aperture Radar (InSAR), have proven instrumental in monitoring land subsidence with high precision and over large areas (Ferretti et al., 2015). For instance, InSAR has been utilized to detect subsidence in Mexico City, where rapid urbanization and groundwater depletion have caused significant ground lowering (Castellazzi et al., 2016), and in the San Joaquin Valley, USA, where agricultural water use has led to extensive subsidence (Jeanne et al., 2019). By integrating InSAR data with other geospatial and environmental datasets, researchers can better understand subsidence patterns, their causes, and their impacts (Liu et al., 2021). This approach allows for developing targeted mitigation strategies, ensuring the sustainability of urban environments worldwide (Amin Khalili et al., 2024).

The city of Tehran, with its unique natural location, regional characteristics, high population density, and dense urban structure, has the potential to experience hazards and create critical conditions. Various studies have shown that the morphological phenomenon of subsidence is occurring and expanding at different rates in this region (Alipour et al., 2008; Motagh et al., 2008; Dehghani et al., 2013; Mahmoudpour et al., 2013, 2016; Haghighi and Motagh, 2019; Babaee et al., 2022). This phenomenon and its effects have been observed in various locations in and around the city, such as the west and southwest, the Varamin plain, Shahriar, and Karaj (Mahmoudpour et al., 2013; Haghighi and Motagh, 2019). Various factors contribute to this subsidence, the most important being the excessive groundwater extraction from aquifers in the region (Motagh et al., 2008). However, other factors, such as urban development plans, underground constructions, civil engineering activities such as renovating the city's aging infrastructure, and different soil characteristics, can also cause localized subsidence in densely populated urban areas with smaller spatial extents (Herrera et al., 2010; Valente et al., 2021).

Therefore, regular monitoring and measurement of surface displacement and its impact on urban infrastructure is one of the significant challenges in managing the Tehran megacity. Unfortunately, the lack of continuous monitoring programs to examine subsidence and land movements in this plain using classical geodetic tools such as permanent Global Navigation Satellite System (GNSS) and leveling has led researchers to turn to the well-known technology of radar interferometry. In this regard, numerous studies have been conducted using various radar satellite data in recent years (Haghshenas Haghighi et al., 2013; Esmaeili et al., 2017; Haghighi and Motagh, 2019; Baniani et al., 2021). Still, the results obtained in terms of the average rate of subsidence in this plain differ in limited cases. The reason for this difference can be attributed to the specific mechanism of subsidence in Tehran and its surroundings, such as changes in subsidence rates in winter and summer, the existence of local subsidence with high rates, and the limitations of interferometric radar technology, such as phase ambiguity and the need for preliminary information to resolve it, temporal and spatial incoherence, errors due to atmospheric signals, and measuring real two-dimensional displacement on the satellite Line of Sight (LoS).

In addition to the above, investigating the dynamics of subsidence in Tehran and its suburbs requires a long-term study to accurately model subsidence behavior in this region. Therefore, the aims of this study are as follows.

- **Review the existing body of knowledge:** We first review the existing knowledge about subsidence triggers and rates in the Tehran Plain.
- **Long-term evaluation:** Focus on the long-term assessment of the spatiotemporal characteristics of subsidence in the city and suburbs of Tehran.
- **Data analysis:** Analyze Sentinel-1A radar images acquired in the framework of the Copernicus project of the European Space Agency (ESA) in ascending and descending tracks from 2016 to the beginning of 2021.
- **Displacement components:** Simultaneously analyze Sentinel-1A radar images to identify vertical displacement components and evaluate their precision.
- **Validation:** Validate the results obtained using the GPS station in our case study.
- **Assessing relationships:** Evaluate the relationship between vegetation distribution, groundwater depth, and subsidence patterns using the Normalized Difference Vegetation Index (NDVI) and the Normalized Difference Moisture Index (NDMI) derived from Landsat 8 OLI/TIRS sensors.

These sensors ensure consistent and extensive coverage throughout the investigated area over the specified period (2015–2020), making them comparable to the subsidence studies carried out with the Sentinel-1A and Landsat 8 OLI/TIRS satellites.

The rest of the research is organized as follows: Section 2 reviews the history of subsidence studies in the Tehran Plain and its suburbs. Section 3 examines the study area from its altitude, geology, and hydrology perspective. Section 4 describes and summarizes the dataset we used. In contrast, the implemented methodology and the processing algorithm are explained in Section 5. Finally, Sections 6,7 and 8 focus on evaluating the results, discussion, and conclusion, respectively.

2. Review of subsidence literature

A comprehensive literature survey on subsidence plays a pivotal role in advancing our understanding of this phenomenon. By examining existing research, we can gain valuable insights, identify gaps in knowledge, refine methodologies, and ensure that new

studies contribute meaningfully to the existing body of information. In this regard, the history of the study of subsidence in the Tehran plain can be summarized as follows.

The first studies that led to the discovery of subsidence in the Tehran Plain were related to reports on changes in groundwater resources and regional geology (Engalenc, 1968). These studies showed a spatial correlation between the location of groundwater recharge and discharge areas and changes in land surface, which, according to research (Masson et al., 2002), could not be attributed to tectonic movements or faults in the region. In addition to geological and hydrological studies, the National Cartography Center (NCC) of Iran, in its first initiative between 1995 and 2000, measured the vertical changes along a series of benchmark lines and recorded an average subsidence of 12.5 cm per year in this plain (Pirouzi and Eslami, 2017). The second set of measurements began in 2001 and continued until 2010, with an increase in the number of benchmark lines measured. The result of this survey estimated an average subsidence rate of 20 cm per year (Pirouzi and Eslami, 2017).

The results and data obtained from these surveys and similar activities conducted by the Geological Survey of Iran (GSI) are not widely available to researchers and have been published in limited reports in Persian (Arabi et al., 2005; Shemshaki et al., 2005; Amighpey et al., 2006). Almost simultaneously, with the implementation of the Iranian Permanent Geodynamic and GNSS network (IPGN) with more than 100 stations in 2005 (Djamour et al., 2007), the NCC established a local geodynamic network in Tehran with a limited number of GNSS stations. In this network, two stations were established in the subsidence-prone area (Mahmoudpour et al., 2016). However, due to the lack of a complete image of the subsidence in the region and the temporary nature of these stations, they could not provide the necessary efficiency in monitoring the spatiotemporal pattern of subsidence in the area. In addition, in recent years, other GNSS networks have been launched in Tehran and its suburbs for geodynamic and geological studies, micro-geodesy, and displacement monitoring of faults, dams, and large structures. Again, though, due to the lack of stations in subsidence-prone areas and

Table 1
A summary of studies conducted on subsidence in the Tehran plain.

Category	Study type	Reference	Used data	Study year	Estimated subsidence
I	Estimating spatiotemporal subsidence pattern and investigating its correlation with changes in groundwater levels.	Pirouzi and Eslami (2017)	Benchmarks Boreholes Piezometric wells	1990–2010	−22 to −36 cm/yr
		Mahmoudpour et al. (2016)	hydraulic head InSAR data	Up to 2018	−30 cm/yr
		Mahmoudpour et al. (2013)	InSAR + GPS +Leveling	2004–2010	−36 cm/yr
		Papi et al. (2020)	Env (Desc)	Jul 2003–May 2010	−27 cm/yr
		Alipour et al. (2008)	Env (Asc + Desc)	2003–2005	−60 cm
		Schenk (2006)	Env (Asc + Desc) ERS (Desc)	2003–2005 1998–1999	~14 mm/ month
		(Baniani et al., 2021; Gourmelen et al., 2003)	ERS (Desc)	Sep 1998–Jun 1999	Uplift >9 cm
		Baniani et al. (2021)	S1A	2018–2019	−11.7 cm/yr
II	Using different radar sensors in subsidence monitoring.	Tarighat et al. (2021)	CSK (Asc + Desc) S1A (Asc + Desc)	Apr 2014–Feb 2016 Apr 2014–Dec 2016	−26 cm/yr −22 cm/yr
		Haghighi and Motagh (2019)	Env (Asc + Desc) ALOS (Asc) TSX (Desc) S1A(Asc + Desc)	2003–2017	> −25 cm/yr
		Haghshenas Haghighi et al. (2013)	Env (Asc + Desc) ALOS (Asc) TSX (Desc)	2003–2005 Jan 2008–Mar 2010 2012–2013	> −20 cm/yr
III	Development of algorithms and selection as the study area.	Babaee et al. (2022)	SA1 (Asc)	Nov 2016–Jan 2018	> −20 cm/yr
		Foroughnia et al. (2019)	S1A (Asc + Desc) Env (Asc)	2014–2017 Aug 2004–Sep 2010	−39.6 cm −88.4 cm
		Azadnejad et al. (2019)	S1A (Asc)	Mar 2017–Oct 2017	−15 cm/yr
		(Ajourlou et al., 2019)	S1A (Asc)	Oct 2014–May 2018	~22 cm/yr
		Esmaeili et al. (2017)	TSX (Asc)	Jul 2013–Jan 2014	-
		Esmaeili and Motagh (2016)	TSX (Asc)	Jul 2013–Jan 2014	−20 to −24 cm/yr
		Dehghani et al. (2013)	Env (Asc + Desc)	Aug 2004–Oct 2008	−20 to −25 cm/yr

Env: Envisat, TSX: TerraSAR, S1A: Sentinal-1A, CSK: COSMO-SkyMed, Asc: Ascending, Desc: Descending.

the unavailability of information on these stations, subsidence studies and modeling using this data have not received much attention and are limited in scope.

In recent decades, with the emergence and advancement of Multi-Temporal Interferometric Synthetic Aperture Radar (MTInSAR) technology in studying ground deformation (Wasowski and Bovenga, 2014) and its acceptable precision compared to other classical geodetic methods, many researchers have been inclined to use this method to estimate the spatiotemporal pattern of subsidence in the Tehran plain. One of the first attempts was made by (Gourmelen et al., 2003). However, the misinterpretation of the results of this study showed that the Tehran plain experienced an uplift of more than 9 cm between 1998 and 1999, which was attributed to the recharge of groundwater aquifers. Another study (Schenk, 2006) corrected the previous results and estimated the subsidence rate in this plain to be −14 mm/month.

Furthermore, with the help of newer radar images, (Motagh et al., 2008; Haghshenas Haghighi et al., 2013; Haghighi and Motagh, 2019) reported subsidence in the Tehran plain and the associated hazards at different time intervals. In addition to these studies, many researchers have conducted similar studies using interferometric radar in recent years, including (Alipour et al., 2008; Dehghani et al., 2013; Esmaeili and Motagh, 2016; Esmaeili et al., 2017; Foroughnia et al., 2019; Maghsoudi et al., 2021; Babaee et al., 2022). Recent research on subsidence in the Tehran plain can be categorized into three groups: I) studies aimed at monitoring and estimating spatiotemporal patterns of subsidence and investigating its relationship with changes in groundwater levels, II) studies aimed at examining the capability of different radar datasets for subsidence monitoring, and 3) studies aimed at developing algorithms and selecting the study area. Table 1 summarizes the studies on subsidence in the Tehran plain in each category mentioned.

A significant point noted in the results of previous InSAR-based studies is the report of different subsidence rates for this plain. The main reason for this issue can be attributed to the difference in the studied periods and the leakage of error caused by ignoring the

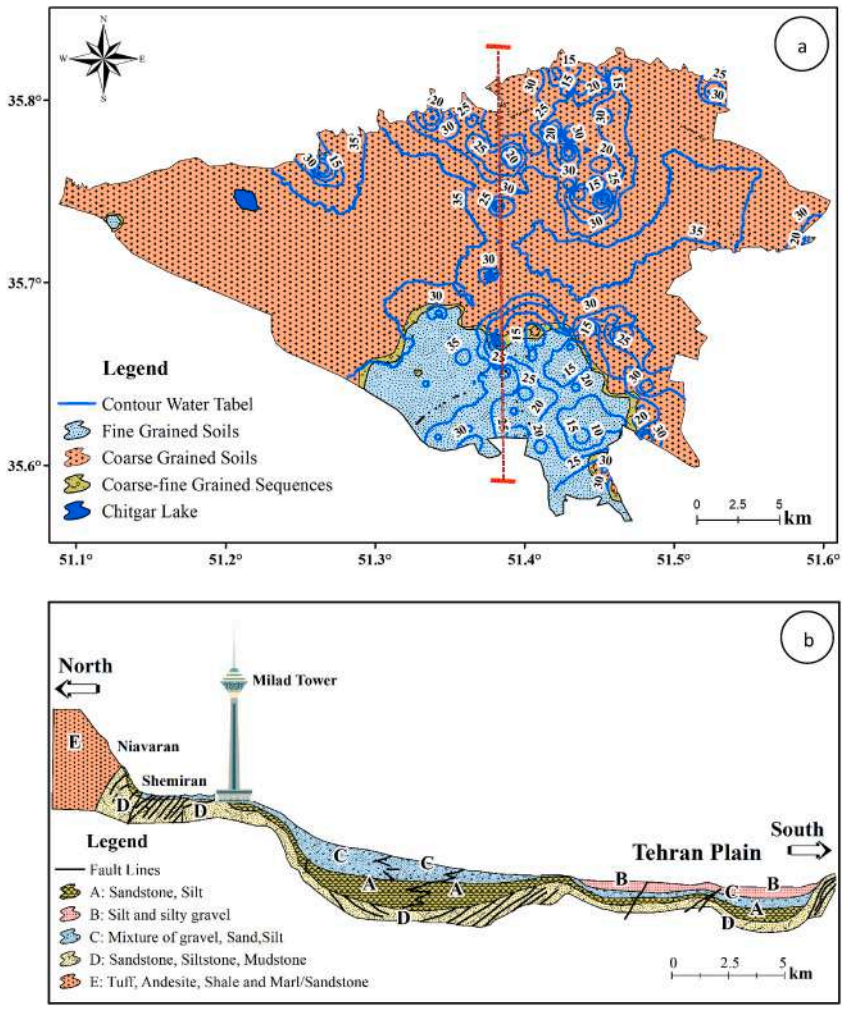

Fig. 1. Simplified soil type distribution map of the Teheran City (Coordinate System: WGS84). a) shows the soil type distribution in the study area based on particle size up to a depth of 15 m (prepared by the Geotechnical and Materials Resistance Studies Center of Tehran). b) shows the geo-lithological section of Tehran city from north to south along the red profile drawn in the top figure. (For interpretation of the references to color in this figure legend, the reader is referred to the Web version of this article.)

effect of horizontal displacement in the final results.

3. Case study

3.1. Topographical setting

Tehran is a mountainous city located at an altitude of 1000–1700 m above sea level. Three distinct elements, including mountains, foothills, and deserts, have shaped the landscape and natural environment of the region. The presence of the Alborz Mountain range in the northern part and the three-legged mountain range in the east has limited the growth of the metropolis of Tehran in these directions, and the city's expansion is more towards the west and southwest. The southern margin of the urban area of Tehran and its suburbs are mainly composed of agricultural areas, including fruit orchards, vegetable gardens, and farms. In addition, in most southern parts of the region (lands with an altitude of fewer than 900 m), we mostly witness the existence of industrial complexes and the new international airport of Tehran.

3.2. Geo-lithological and hydrological setting

The study area is located in the Central Alborz and Central Iran geology structural units (Ahadnejad et al., 2016). The northern part of the area has Alborz structural features, while the southern and south-eastern parts include the structural features of Central Iran and Tehran plain. The north Tehran fault is the boundary between these regions, where the Alborz mountains slide onto the Tehran plain. Despite some structural similarities between these regions, they differ significantly regarding geo-lithology and soil types. The northern and foothill areas have alluvial soil, formed from gravel in the upper and clay and sand in the lower parts. The soil in the central and southern parts of Tehran is mainly fine-grained, while the northern parts of Tehran have coarser soil. Fig. 1 shows Tehran city's soil type distribution map based on the particle size up to a depth of 15 m. It highlights the distinct nature of the soil in southern Tehran, particularly in the subsidence-affected areas, where the highest number of sinkholes can be found. The soil elements in this area have been formed from different proportions of debris particles such as boulders, sand, silt, and clay. The particle diameter gradually decreases from the margin towards the central and southern parts of the plain. Most areas of Tehran city, especially the northern and northwest regions, are characterized by coarse sediments that are not necessarily susceptible to subsidence. However, some local subsidence (i.e., settlement) in these areas may be due to the local fine-grained layers or infrastructure activities (Ahadnejad et al., 2016; Mahmoudpour et al., 2016).

From a hydrological perspective, Tehran has a semi-arid climate with approximately 257 mm of mean annual precipitation (Pirouzi and Eslami, 2017). However, the peaks and northern slopes experience high humidity, with the predominant form of precipitation being snow, totaling more than 2000 mm per year. Urban development has also been shaped more by access to water resources. Surface water in the region flows towards the desert through several rivers and streams seeping into the foothills' thick alluvial layers. To provide a broader context before focusing on the specific area of Tehran, it is essential to discuss related studies on water dynamics and anthropogenic impacts in Iran. For instance, Taheri Dehkordi et al. (2022) investigated the surface water dynamics in the reservoirs of Iranian dams and studied their relationships with climate using Landsat imagery and machine learning models in the Google Earth Engine (GEE) platform. This study highlights the significant role of remote sensing and advanced data analysis techniques in monitoring water resources.

Similarly, Maghrebi et al. (2023) examined trends in river flow across Iran, documenting the effects of anthropogenic activities on water discharge. Their research underscores the impact of human interventions on natural water systems, providing valuable insights into the broader implications of water management practices in the region. These studies collectively illustrate the importance of understanding natural and human-induced factors in water resource management, setting the stage for our investigation into land subsidence in Tehran.

In contrast, Tehran's drinking water is mainly supplied through the large dam systems built on the Karaj, Jajrood, Lar, and Taleghan rivers. Due to the influx of urban sewage and groundwater movement, the water table in the central and southern parts of Tehran is higher than in the northern regions. The groundwater table depth in the northern areas can reach up to 130 m, up to 120 m in the northeast, and up to 100 m in the northern of the plain (Schenk, 2006). The groundwater depth decreases towards the south of the study area, reaching as low as 10 m due to the increase in fine-grained aquifer tissue (Mahmoudpour et al., 2016). Studies suggest the existence of three confined aquifers in the southern part of Tehran, mainly composed of silt and clay soil (Mahmoudpour et al., 2016). Among these aquifers, the one that supplies most of the groundwater resources starts from a depth of approximately 60 m and has a thickness of 2–20 m. Generally, the depth of the aquifers ranges from 20 to 100 m, depending on the topographic gradient of the region, with deeper aquifers found in the southern plain areas and shallower aquifers in the foothill regions (Haghighi and Motagh, 2019).

The elevation of the Bedrock of the study area varies from 1400 m in the northern parts to 400 m in the southern parts, where the aquifers are located (Shirzad and Hossein Shomali, 2014). Unregulated extraction of groundwater and the presence of various dams constructed in river channels for collecting surface water are the two main factors contributing to the decline in the groundwater level of the aquifers in Tehran plain, with the groundwater level dropping by 12 m between 1984 and 2011 (Haghighi and Motagh, 2019). However, most groundwater extraction is used for agricultural, park irrigation, and industrial purposes, with contamination and the effects of the traditional septic well system for wastewater disposal in Tehran being one of the main reasons. Although development plans and implementation of sewage canals have started in recent years, a large portion of the city still uses the traditional absorption well system (Karamouz et al., 2004).

4. Data sets

In this study, the C-band radar SAR images of the Sentinel-1A satellite have been used. This satellite began its mission in April 2014 and was able to significantly improve the time interval between radar images of a region and provide better coverage of the area. The history of all radar images taken by this satellite in the study area from the beginning of 2016 to early January 2021 for the ascending and descending orbits is shown in Fig. 2.

The radar data used in this paper consists of two datasets in ascending and descending orbits with a short temporal resolution (approximately 12 days) from the second month of 2017 onwards. Track number 35 (T35) includes 129 radar images taken in the descending orbit from January 6, 2016, to January 3, 2021. Track number 28 (T28) also contains 123 radar images taken in the ascending orbit from January 19, 2016, to January 4, 2021. The imaging mode for these images is the terrain observation by progressive scans (TOPSAR) advanced imaging method, obtained using interferometry with synthetic aperture radar technique (De Zan and Guarnieri, 2006) for interferometric wide (IW) swath single look complex (SLC) applications. More details about the radar images used in this study are shown in Table 2.

To avoid computational load, we have focused on a small region within the Tehran metropolitan area covered by both sets of radar data from the ascending and descending orbits. This selection of a smaller study area allowed for efficient data processing and reduced computational burdens that would have been required for analyzing more significant regions. The chosen study area is shown in Fig. 3, which indicates the boundaries of the region of interest.

This study also uses a multispectral image dataset produced by the Landsat 8 OLI/TIRS sensors provided by the U.S. Geological Survey (USGS) to assess the relationship between the spatial variation of vegetation, groundwater depth, and subsidence. (See more information in Table 2). The image collection function uses the open-source and cloud-based Google Earth Engine (GEE) platform. The Landsat Level 2, Collection 2, and Tier 1 (i.e., "LANDSAT/LC08/C02/T1_L2″) image collection provided by GEE is composed of atmospherically corrected surface reflectance (SR) and land surface temperature multispectral data. Using the Land Surface Reflectance Code (LaSRC) version 1.5.0 model (Vermote et al., 2016; *Landsat Collection 2 U.S. Analysis Ready Data*, 2023). The 30 m/pixel spatial resolution Landsat 8 data have five Visible Near Infrared (VNIR), two Shortwave Infrared (SWIR) bands, and one thermal infrared (TIR) band processed to orthorectified surface temperature.

To make the dataset more robust and account for the comparison of more variables for interpretation purposes, cumulative total precipitation data obtained from the land component of the fifth generation of European ReAnalysis (ERA5), called ERA5-Land

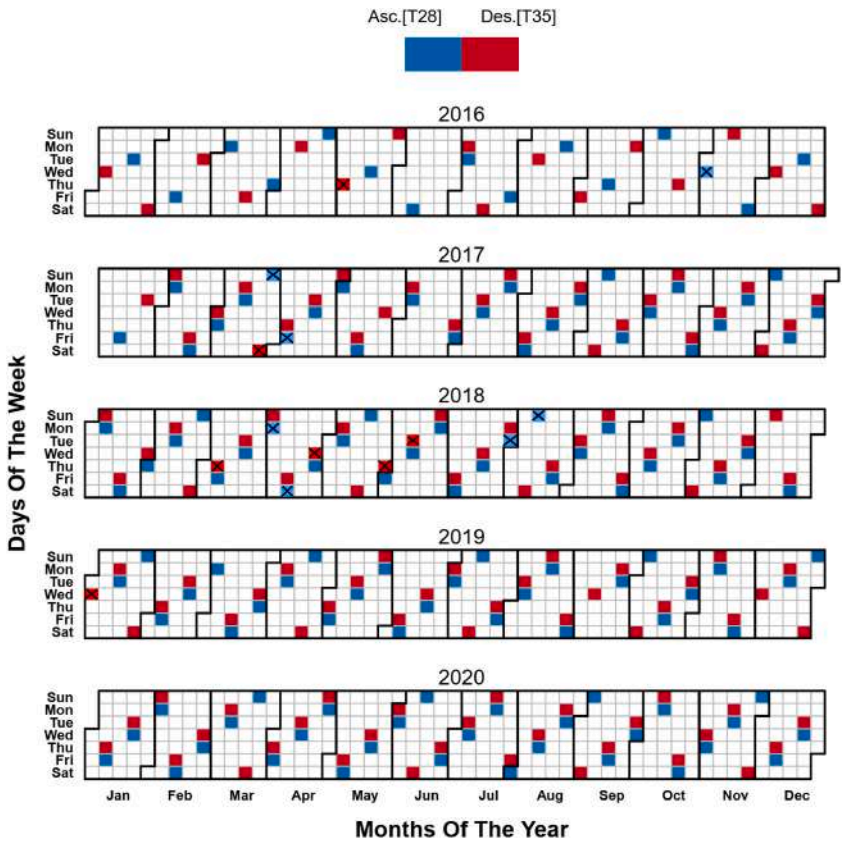

Fig. 2. A chronological timeline of radar images obtained by the Sentinel-1A satellite from the study area. Blue and red squares represent images taken in the ascending and descending orbits, respectively. Images marked with a drawn line were not included in the processing. (For interpretation of the references to color in this figure legend, the reader is referred to the Web version of this article.)

Table 2
A summary of the datasets (Sentinel-1A SAR dataset and multispectral Landsat 8 OLI/TIRS image collection) used in this study.

Radar data	Orbit	Imaging mode	Time interval	Number of images	Azimuth angle (degree)	Mean incidence angle (degree)
SA1-Track 28 (T28)	Ascending	IW, SLC	Jan 2016–Jan 2021	123	350	41
SA1-Track 35 (T35)	Descending	IW, SLC	Jan 2016–Jan 2021	129	190	38
Landsat 8 OLI/ TIRS	–	LC08/C02/ T1_L2	Jan 2015–Oct 2021	222	139.5	Nadir

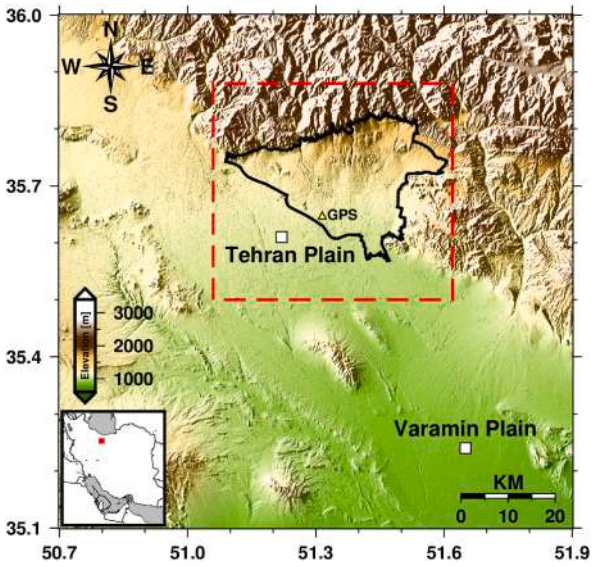

Fig. 3. Tehran Plain's study area and shaded relief map, derived from the SRTM 30-m digital elevation model. The bold black border and red dashed line indicate the Tehran metropolitan area and our study area, respectively. The yellow triangle shows the location of the GPS station, and the red square in the lower-left corner of the figure indicates the geographic location of the study area in Iran. (For interpretation of the references to color in this figure legend, the reader is referred to the Web version of this article.)

reanalysis (pre-calculated daily aggregates), was used in GEE. It is released by the European Centre for Medium-Range Weather Forecast (ECMWF) and generated under the framework of the Copernicus Climate Change Service (C3S) (Muñoz-Sabater et al., 2021) and represents a globally consistent and comprehensive reanalysis dataset, which offers a view on the long-term changes in land variables spanning several decades (available since July 1963) at an improved resolution compared to ERA5.

5. Methodology

5.1. Interferometry processing method

The interferometric time series analysis was performed in two main steps, similar to the algorithm shown in Fig. 4. The first step is to create a stack of interferograms with the unwrapped phase. The second step is to perform a time series analysis and filter errors to estimate the displacement rate map and time series of displacement points.

In the first step, the large stack of interferograms is generated, and the Minimum Cost Spanning Tree (MCST) method (Fattahi et al., 2016) is used to produce the interferograms with the unwrapped phase. In the second step, the time series analysis is performed on the stack of interferograms using the Small Baseline Subset (SBAS) technique (Berardino et al., 2002) and the Singular Value Decomposition (SVD) method (Wall et al., 2003) to estimate the displacement rate map and time series of displacement points. The displacement time series are then converted to the up-down and east-west components using the satellite's LoS direction.

5.2. Implementation of interferometric time series analysis and settings

We used the open-source InSAR Scientific Computing Environment (ISCE) software (Rosen et al., 2011) to process raw Sentinel-1A SAR data. This software uses a stack processor to register all slave images to a master image geometrically and generate the stack of interferograms with the unwrapped phase. In the second step, the stack of interferograms with the unwrapped phase, which forms a fully connected network, is used as input to the Mintpy software for time series analysis using the short baseline approach. MintPy is another open-source software package for MTInSAR data processing and provides similar functionalities to ISCE (Yunjun et al., 2019).

Based on the above discussion, for geometric registration of SAR images concerning a reference image in ISCE software, the image

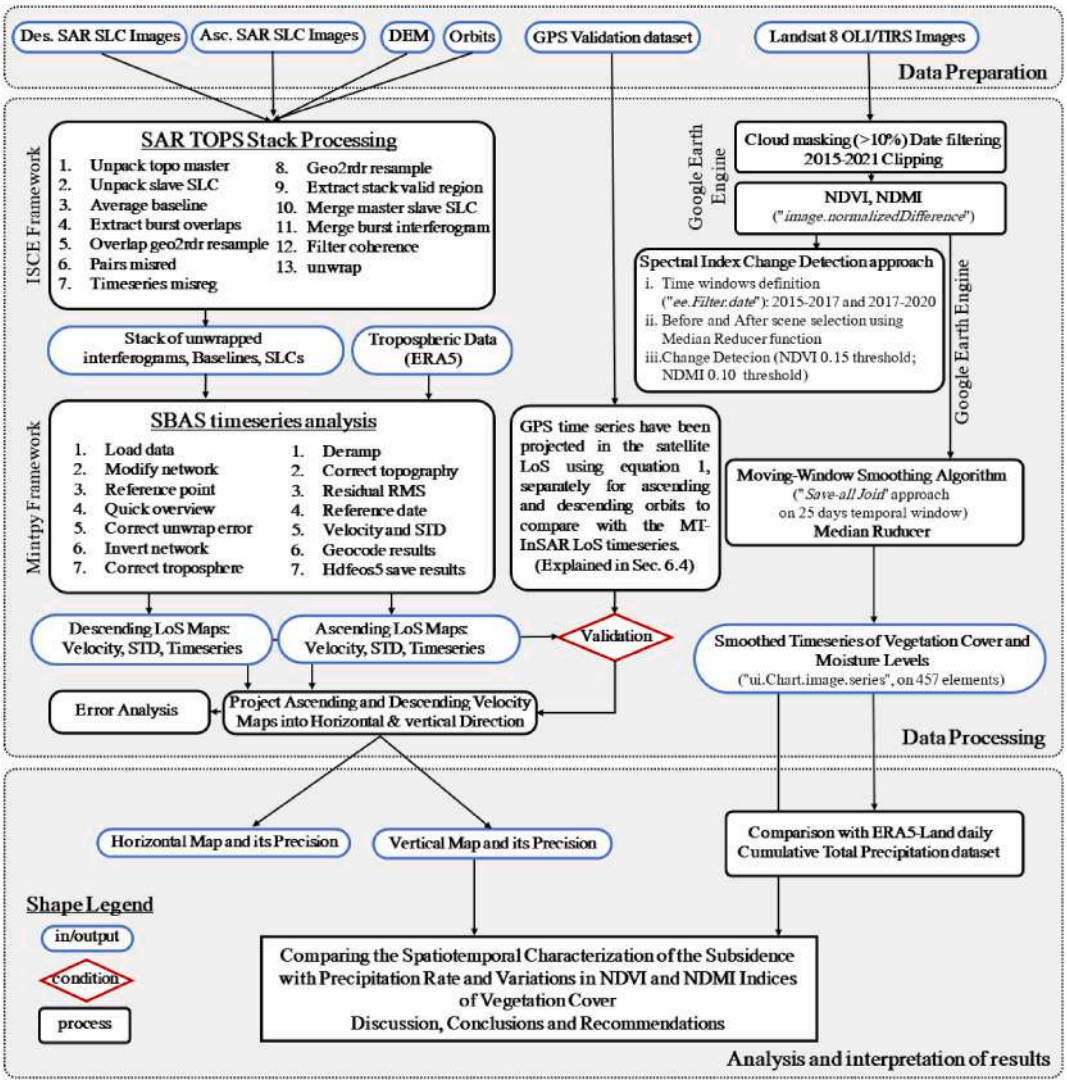

Fig. 4. General research methodology flowchart.

of November 3, 2018, in the ascending orbit and the image of November 4, 2018, in the descending orbit were selected as reference images. These images were chosen to have shorter spatio-temporal baselines compared to all other images to increase coherence. After the geometric registration of all images concerning the reference image, each SAR image is paired with its two nearest temporal neighbors to form an interferogram stack (sequential connectivity network). Note that increasing this number significantly increases the computational load due to network complexity. SRTM digital elevation model with an approximate resolution of 30 m is used to remove the phase component caused by topography and assist in the geometric registration process.

Additionally, to create multi-looking interferograms, window sizes of 5 and 15 are chosen in azimuth and range directions, respectively. Phase filtering uses a Goldstein filter with a power of 0.5 on the interferograms, and phase unwrapping is done using the SNAPHU method. As seen in the interferogram network in Fig. 5, due to the short spatio-temporal baselines between images, the mean coherence coefficient of the created interferograms for ascending and descending orbits is higher than 0.65. The total number of created interferograms is 494, of which 255 belong to the ascending orbit and 239 belong to the descending orbit.

The time series analysis stage used Mintpy software, ERA-5, and the ERA-Interim weather model to remove the tropospheric phase effect. The remaining tropospheric phase, ionospheric delay, and orbit ramp error were subtracted from the phase of each interferogram using a linear relationship. Additionally, the phase error due to topography was calculated using a linear polynomial with a vertical baseline time series ratio for each pixel.

After performing time series analysis and generating displacement rate maps along the satellite LoS for ascending and descending orbits and their mutual validation, the horizontal and vertical displacement fields are retrieved. Finally, their precision is examined, which will be discussed in detail in the next section.

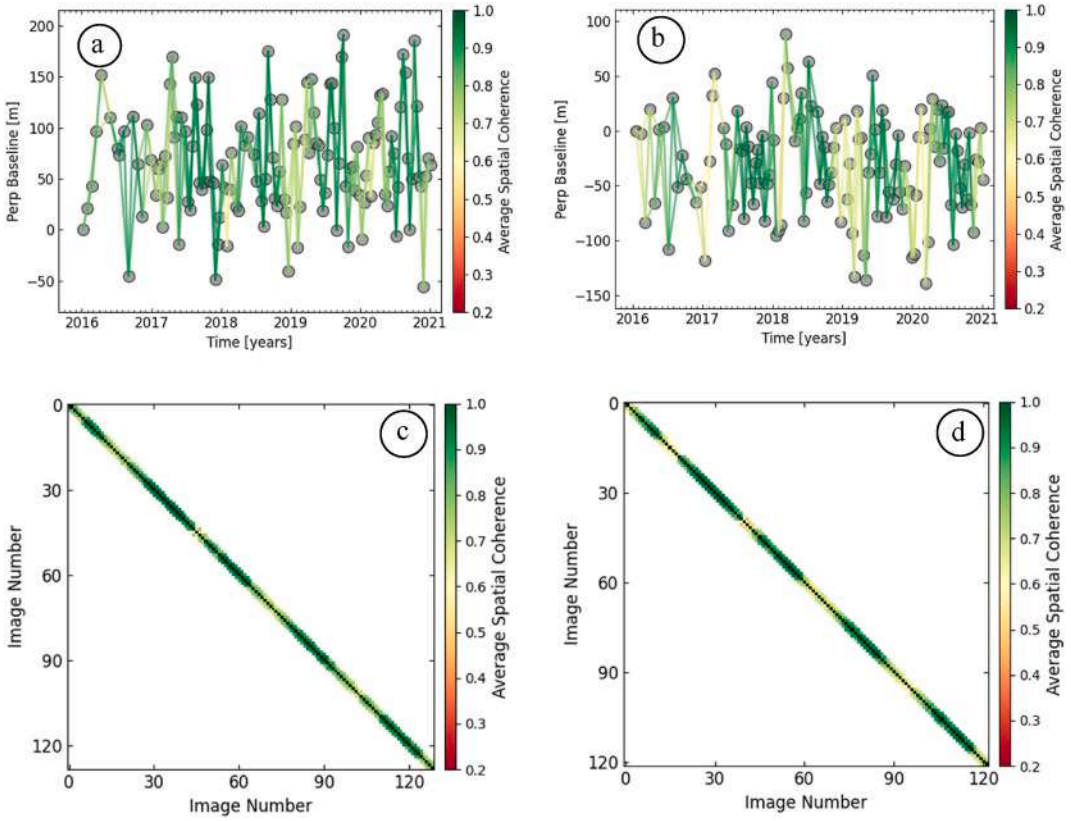

Fig. 5. A sequential network of interferograms is created in the short baseline method, where gray dots indicate the radar images used, and the connecting lines represent the generated interferograms between each pair of images. The color of the connecting lines indicates the corresponding interferogram's mean coherence. a) ascending orbit, b) descending orbit. c) spatial coherence matrix of the interferogram network in the ascending orbit, and d) spatial coherence matrix of the interferogram network in the descending orbit. (For interpretation of the references to color in this figure legend, the reader is referred to the Web version of this article.)

5.3. *Recovering the horizontal and vertical components of displacement rates and their precision*

The displacement rate obtained from the time series analysis in the satellite LoS direction is composed of the real horizontal and vertical components of the displacement rate field, and for each pixel, its equation can be written as follows (Hanssen, 2001):

$$V_{LOS} = V_{UD}\cos\theta - \sin\theta.(V_{EW}\cos\alpha - V_{NS}\sin\alpha) \pm \varepsilon_{LOS} \tag{1}$$

Where V_{NS}, V_{EW}, V_{UD} are the three components of the real 3D displacement field, represented by the up-down (vertical), east-west, and north-south components, respectively. Also, α is the satellite azimuth angle, θ is the satellite viewing angle concerning the nadir direction, V_{LOS} is the observed displacement along the satellite LoS direction, and ε_{LOS} is the measurement error in the displacement rate. Due to the low sensitivity of radar observations to the displacement component in the north-south direction (Hanssen, 2001) and based on previous studies (Haghighi and Motagh, 2019; Babaee et al., 2022), we assume that the displacement in this direction is negligible and set the third term in equation (1) to zero, resulting in the following rewritten equation.

$$V_{LOS} = V_{UD}\cos\theta - V_{EW}\sin\theta\sin\left(\alpha - \frac{\pi}{2}\right) \pm \varepsilon_{LOS} \;\; ; \;\; V_{NS} = 0, \tag{2}$$

If there are at least two radar observations in ascending and descending orbits for each pixel, equation (2) can be rewritten in matrix form for the corresponding pixel (Motagh et al., 2017).

$$\begin{pmatrix} V^a_{LOS} \\ V^d_{LOS} \end{pmatrix} = \underbrace{\begin{pmatrix} \cos\theta^a & \sin\theta^a\sin\left(\alpha^a - \frac{\pi}{2}\right) \\ \cos\theta^d & \sin\theta^d\sin\left(\alpha^d - \frac{\pi}{2}\right) \end{pmatrix}}_{A} \begin{pmatrix} V_{UD} \\ V_{EW} \end{pmatrix} \pm \begin{pmatrix} \varepsilon^a_{LOS} \\ \varepsilon^d_{LOS} \end{pmatrix} \tag{3}$$

Here, the superscripts *a* and *d* refer to the ascending and descending geometries, respectively. The presence of any noise in the ascending and descending data affects the estimation of the vertical and horizontal displacement components. Assuming that the standard deviation (STD) of phase noise for each pixel in these two orbits is σ^a_{LOS} and σ^d_{LOS} , respectively, the expected accuracy for

estimating the vertical and horizontal displacement components can be calculated as follows.

$$Q_p = \left(A^T Q_{LOS} A\right)^{-1} \tag{4}$$

In this context, Q_p is the covariance matrix of the propagated error, A is the coefficients/design matrix, and Q_{LOS} is the covariance matrix of the initial error. Assuming no correlation exists between displacement components along the satellite LoS, the covariance matrix of the initial error is defined as follows.

$$Q_{LOS} = \begin{pmatrix} \sigma^2_{LOS,a} & 0 \\ 0 & \sigma^2_{LOS,d} \end{pmatrix} \tag{5}$$

In this study, the variance components (the main diagonal of equation (5)) for each pixel in ascending and descending orbits were calculated using the bootstrapping method (Efron and Tibshirani, 1985). In most studies conducted in this area, the contribution of the horizontal displacement component is neglected, and the displacement along the satellite LoS is converted to the vertical displacement (subsidence) by dividing it by the cosine of the satellite incident angle. However, the maximum error caused by displacement along the satellite LoS, without considering the horizontal displacement component, is calculated as follows (Samieie-Esfahany et al., 2009):

$$\varepsilon^{max}_{up} = d^{max}_{horiz.} \tan\theta \tag{6}$$

Here, ε^{max}_{up} the maximum error in retrieving the vertical component of displacement, $d^{max}_{horiz.}$ the maximum displacement in the horizontal component, and θ the satellite incident angle are presented.

5.4. Landsat 8 data processing

As mentioned in the dataset section, an image collection of Landsat 8 imagery covering the study area with a spatial resolution of 30m was processed through the GEE platform, allowing simultaneous analysis of many images online. The pre-processing steps included, firstly, cloud masking, using the Fmask algorithm based on the Quality Assessment (QA) bands that use quality bands of Landsat 8 to mask out any pixels that are either obscured by clouds and cloud shadows or are saturated, ensuring a cloud pixel percentage lower than 10% (Taheri Dehkordi et al., 2022). Secondly, filtering by date was performed from 2015 to 2021. A dataset composed of 222 images was selected for the processing. The images were then clipped for the study area of interest.

Subsequently, the NDVI and the NDMI indexes were extracted through the *image.NormalizedDifference function in GEE is used* to investigate the relationship between the spatial distribution of vegetation and moisture levels in vegetation and soil in the areas characterized by higher linear displacement rates. The algorithm computes the normalized difference between two Landsat 8 bands: NIR (850–880 nm, Band 5 in Landsat 8) and RED (530–590 nm, Band 4 in Landsat 8) for the NDVI (Exp. 7); NIR and SWIR 1 (1570–1685 nm, Band 6 in Landsat 8) bands are used for the NDMI (Exp. 8).

$$NDVI = \frac{NIR - RED}{NIR + RED} = \frac{\text{Band}_5 - \text{Band}_4}{\text{Band}_5 + \text{Band}_4} \tag{7a}$$

$$NDMI = \frac{NIR - SWIR1}{NIR + SWIR1} = \frac{\text{Band}_5 - \text{Band}_6}{\text{Band}_5 + \text{Band}_6} \tag{8}$$

Time series of the vegetation cover and moisture levels were extracted using the *ui.Chart.image.series* function for NDVI and NDMI results referring to the selected areas. To enhance the visual representation, a moving-window smoothing algorithm, constructed on a 25-day temporal window, was employed to reduce fine-grained variations between time intervals in time series data, which often exhibit abrupt fluctuations due to seasonal influences and other disturbances in the input image. The moving-window smoothing technique (Li et al., 2021) performed in GEE utilizes a "Save-all Join" approach, where the primary image collection is combined with itself, and all images falling within the temporal window are incorporated as a property of each image. Subsequently, a median reducer function was applied to all the images, resulting in the median pixel value within the given timeframe (Taheri Dehkordi et al., 2022). The resulting time series are smoothed for sharp peaks and valleys, rendering it more resilient against anomalies such as cloudy/obscured pixels. To highlight the changes in vegetation distribution and moisture levels as indicated by NDVI and NDMI, we employed a single band/spectral index change detection approach. This analysis utilized Landsat 8 imagery from two distinct periods: 2015–2017 and 2017–2020. Image processing was performed within the GEE platform, and the "ee.Filter.date" filter was used to specify date ranges within the same pre-processed image collection used in the previous analysis. The "before" and "after" images were created by computing the NDVI and NDMI indices based on median values of images captured between September 1 and September 15 of each year. This period was chosen because it is typically less influenced by rainfall and seasonal variations, making it suitable for highlighting non-seasonal vegetation changes. A threshold of 0.15 was applied to the change detection image generated from NDVI, while a threshold of 0.1 was set for the NDMI results.

6. Results

6.1. Spatiotemporal subsidence pattern map

The results show that the average maximum subsidence estimated in the satellite LoS direction for ascending and descending orbits is 18 cm/year. The maximum subsidence occurred in the Shahr-e-Ray and Malard regions, located in the western part of the Tehran

Plain, and the north of Islamshahr (Chahardangeh), in the eastern part of the Tehran Plain.

To better interpret the obtained results, the subsidence components (east-west and vertical displacement) were separated using the results of these two orbits. The satellite viewing angle was first extracted for all pixels and using the azimuth angle of the satellite in both directions, equation (2) was used to calculate the up-down and east-west displacement. As shown in Fig. 6, the average maximum subsidence rate and east-west displacement were estimated to be more than 20 cm/year and 8 cm/year, respectively.

The tectonic activity around the Tehran area gives rise to an NNE-SSW transgressional regime. GNSS measurements reveal NNE-directed shortening at a rate of 5 ± 2 mm per year. Additionally, range-wide shearing occurs at a rate of 4 ± 2 mm per year, associated with left-lateral movements along E-W striking structures (Vernant et al., 2004). However, as depicted in Fig. 6b, most horizontal displacement signals are confined to the subsidence region and do not significantly contribute to the overall tectonic displacement of the area, which exhibits a long spatial wavelength. These horizontal displacements align with the gradient created by the subsidence process and are oriented toward the center of the subsidence zone.

The horizontal displacement map contains some displacement signals with maximum values at the boundaries of the subsidence area but very small horizontal displacements in the central part of the subsidence area (Fig. 6b). The majority of horizontal displacements at the subsidence areas' margins indicate that these movements are located in areas of slope or stress under subsidence. Therefore, the displacement gradient in these areas is expected to be maximum. Considering that the risk of infrastructure damage in areas with subsidence gradients is higher than in other areas, we expect that existing structures are more vulnerable in these areas. In fact, the risk of damage to infrastructure and buildings is greater at the boundary of the subsidence area than in other areas.

In the same way, shown in Fig. 6, except for the south and southwest subsidence of Tehran, there are no significant subsidence signals in other areas, and most subsidence is concentrated in these areas. Subsidence in this area has spread in the shape of an oval with the longer axis in the east-west direction, and areas with the highest subsidence are located in the north of the longer axis of this oval.

Signals with displacement rates greater than −2 cm/year have been removed to visualize subsidence in the study area better, as shown in Fig. 7a. Additionally, since several local areas have the highest subsidence values in the Tehran plain, five specific cross-sectional profiles (locations of these sections are shown in Fig. 7a) have been selected for cumulative ground subsidence analysis during the study period. As shown in Fig. 7b, the maximum cumulative subsidence is observed in profiles C1C2 and E1E2, with values of approximately 100 cm and 88 cm, respectively. For the A1A2 cross-section, which covers the majority of subsidence in the urban area, the maximum cumulative subsidence is approximately 60 cm, located in the southern part of the profile near the Azadegan Highway. Additionally, the subsidence gradient decreases as we move towards the city's central areas along this profile. On the other hand, in the adjacent profile of B1B2, as we move towards the north and urban areas, the subsidence gradient increases. Overall, over time, the subsidence of each point along the direction and slope of the center of the subsidence zone gradually increases, and a continuous bowl-shaped subsidence pattern forms in the local scale, which is compatible with ground subsidence in the study area.

To estimate the precision of the displacement components for each pixel in the vertical and horizontal components, equation (4) was utilized. As shown in Fig. 8, the vertical component's obtained precision is 0–2.3 mm per year, with an average of 0.5 mm per year. Similarly, the precision range for the horizontal component is between 0 and 2.8 mm per year, with an average of 0.6 mm per year. The maximum error in some areas may be due to non-linear displacements or errors in phase retrieval.

It should be noted that, based on the maximum absolute value of the displacement rate in the horizontal component (i.e., equation (6)), which is approximately 80 mm per year, and the average incident angles of the satellite in the ascending and descending orbits, which are 41.77 and 37.15° respectively, the maximum error in calculating the vertical displacement rate component, assuming neglecting the horizontal displacement rate component according to equation (6), is approximately 70 and 61 mm per year for the ascending and descending orbits, respectively. So, here, we show the main consequences of ignoring horizontal displacements in the resulting interpretation. As a result, horizontal displacement is a significant part of our case study's deformation field, and it is not

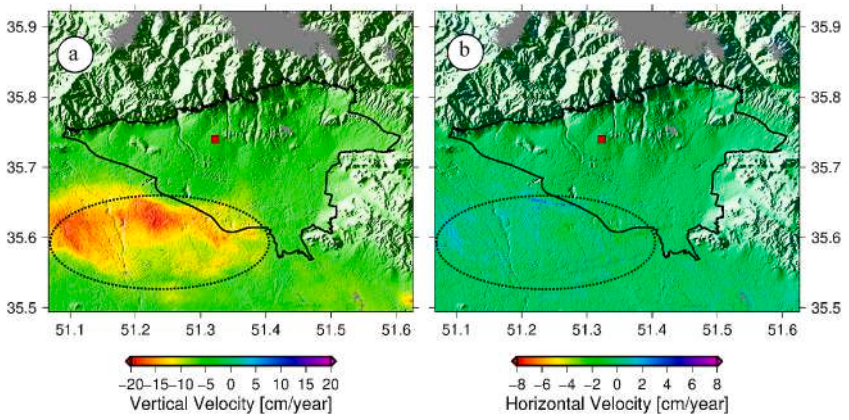

Fig. 6. Linear displacement rates were calculated in the study area using Sentinel-1A ascending and descending radar images (January 2016 to January 2021). (a) Displacement rate in the up-down direction. (b) Displacement rate in the east-west direction. The red square indicates the location of the reference point. (For interpretation of the references to color in this figure legend, the reader is referred to the Web version of this article.)

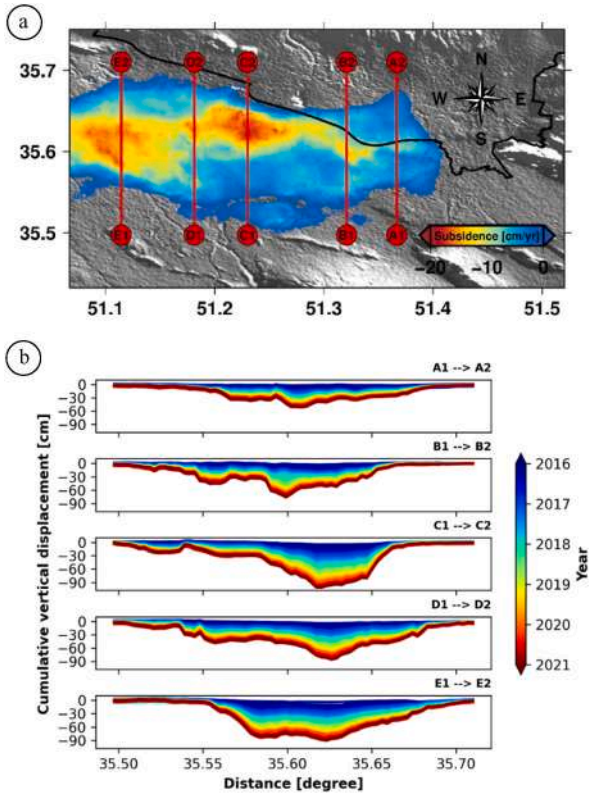

Fig. 7. a) Location of the five specific cross-sectional profiles (red lines) on InSAR-derived subsidence rate map (January 2016 to January 2021), b) spatiotemporal cumulative subsidence profiles along the selected profiles. (For interpretation of the references to color in this figure legend, the reader is referred to the Web version of this article.)

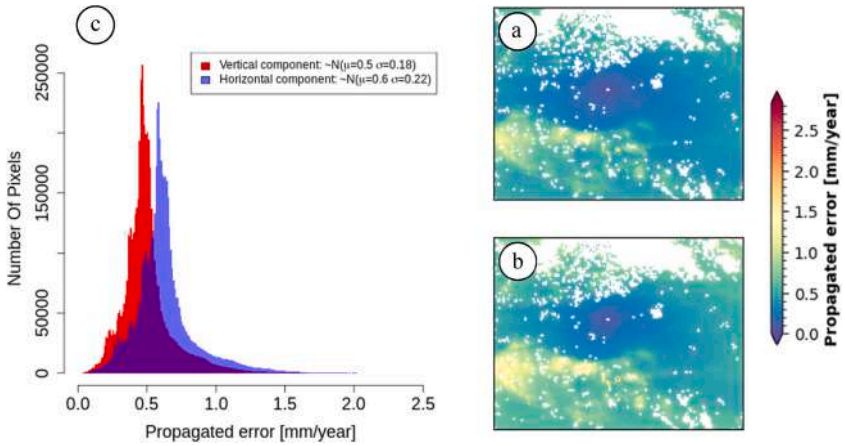

Fig. 8. Error propagated in the direction of components a) up-down b) east-west. c) histogram of propagated errors.

reasonable to ignore it.

6.2. *Time series of Landsat 8 image processing*

Fig. 9 shows the results of the multi-temporal analysis of both NDVI and NDMI over 2015–2021 in selected areas located within the Shahr-e-Ray and Malard regions, as they were affected by the significant subsidence. The gray dots in both graphs are the actual NDVI and NDMI values at specific time instances (as indicated on the x-axis), while the green and red curves, respectively, represent the smoothed interpolation of these values obtained using the moving-window approach. Such indices display a positively correlated pattern, characterized by a pronounced seasonality with increasing NDVI values during the green-up phase from spring to autumn and

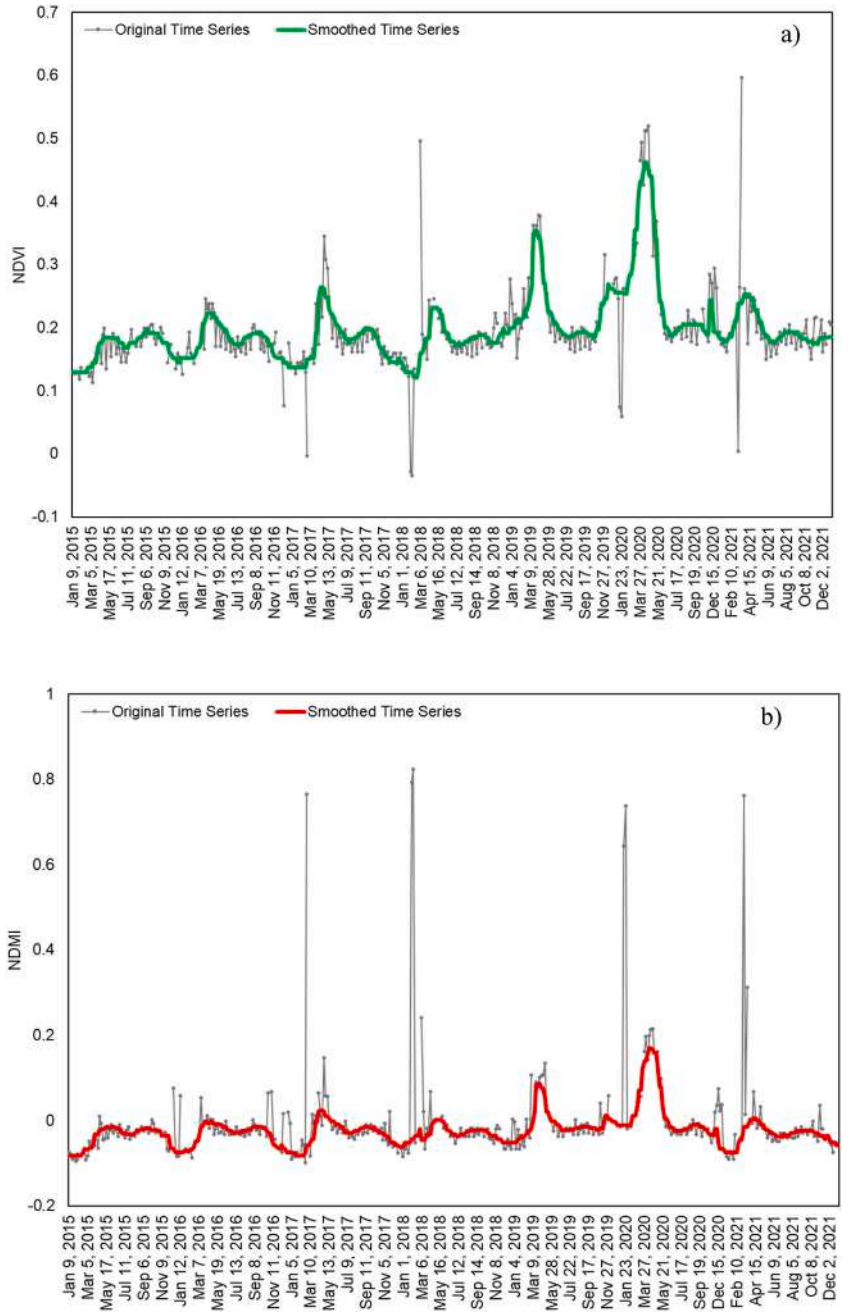

Fig. 9. a) NDVI temporal variations for the time interval of 2015–2021 for the selected zones surrounding the Tehran metropolitan area. The original data, shown as gray lines, are compared to smoothed data (green line) resulting from the moving-window approach; b) NDMI temporal variations for the time interval of 2015–2021 for the selected zones surrounding the Tehran metropolitan area. The original data, shown as gray lines, are compared to smoothed data (red line) from the moving-window approach. (For interpretation of the references to color in this figure legend, the reader is referred to the Web version of this article.)

decreasing NDVI values during the senescent phase from late autumn to winter. Consequently, NDMI also exhibits increasing and decreasing values during these periods, as higher green vegetation generally corresponds to greater moisture levels in vegetation and soil; on the contrary, lower vegetation corresponds to lower moisture availability. Additionally, the cyclic trend observed in both indices appears to follow the seasonal subsidence pattern, with higher subsidence values during dry periods (mainly from January to March) associated with increased water extraction and/or decrease of precipitation rate leading to a decrease in the indices, and lower subsidence values during the summer periods.

Despite the seasonal trend, both indices exhibit a nearly stationary trend during 2015–2016, with maximum NDVI values around 0.2 and NDMI values close to 0. Subsequently, there is a progressive increase from 2017 to 2021, reaching a peak in 2020,

characterized by maximum values of NDVI around 0.5 and of NDMI approximately 0.2. This pattern suggests that there has been an increase in vegetation cover and moisture levels in vegetation and soil since 2017. These results seem to confirm what was found through the InSAR technique, which showed a slowdown in the subsidence rate since 2017. The increase in these indices could be related to a rise in groundwater levels that counteract the ongoing subsidence phenomenon, as verified in other publications (Coda et al., 2019).

6.3. Results evaluation

In this section, two methods were used to validate the MTInSAR-derived results. The first method is the cross-correlation between the displacement rate maps obtained from the ascending and descending orbits. The second method compares with data collected by GPS stations as another independent geodetic source.

Comparing the displacement between measurements in ascending and descending orbits or even the results obtained from different sensors is a common method for examining the compatibility between measurements (Haghighi and Motagh, 2019). Therefore, to demonstrate the self-consistency between the measurements obtained from two different geometries, we compared the mean displacement rates maps in two different geometries for a common area with each other. Fig. 10 shows the correlation between the two datasets in the study area. The two maps of displacement rates in the direction of the satellite LoS in this area were compared for all common pixels in both paths. Then, the distribution of subsidence rates for both paths was compared, which shows that the mean value of root-mean-square error is 2 cm/year, and the correlation coefficient between the estimated displacements (R2) is more significant than 0.96. These values indicate that the two subsidence patterns (average rate) obtained from different datasets are correlated with each other and are influenced mainly by vertical motion.

6.4. GPS-based evaluation

Only the available GPS station in the subsidence area has been used to evaluate the results of the time series analysis of MTInSAR observations. This station is at 35.64° north latitude and 51.29° east longitude. The continuous observations of the station from 2014 to the beginning of 2021 have been collected daily, which coincides with the period of collecting the SAR data used in this study. The station's position can be seen in Fig. 3 (yellow triangle).

To compare the GPS displacement components in the east-west, north-south, and up-down directions with the MT-InSAR components, the GPS time series have been projected in the satellite LoS using equation (1), separately for ascending and descending orbits. Also, the GPS data were temporally interpolated for each MTInSAR epoch using linear interpolation. Therefore, to quantify the agreement between the GPS and InSAR time series, we assume that the GPS time series represents the valid data, and we calculate the correlation coefficient of the InSAR time series concerning the GPS time series. In addition, the root mean square error (RMSE) is obtained using the following equation to calculate the separation between the two InSAR and GPS time series.

$$RMSE = \sqrt{\frac{\sum_{i=1}^{N^{SARs}} \left(d^{i}_{InSAR} - d^{i}_{GPS}\right)^{2}}{N^{SARs} - 1}} \tag{7b}$$

Where d_{InSAR} and d_{GPS} are the LoS displacement values for the MT-InSAR and GPS at time i, respectively, and N is the number of MTInSAR epochs. To provide a more accurate comparison, two lines have been fitted to the measurements obtained from the MT-InSAR and GPS time series using a moving average filter. The pattern and slope values of the fitted lines between the results obtained from the two data sets confirm their compatibility.

Our analysis confirmed the reliability of the displacement rates and correlations between the S1A SAR data and GPS measurements. We calculated the 95% Confidence Intervals (CIs) and P-values for the RMSE values to provide a more comprehensive understanding of the precision and statistical significance of our findings (Table 3).

As can be seen, the spatial pattern of the cumulative displacements obtained by the MTInSAR technique is generally consistent with

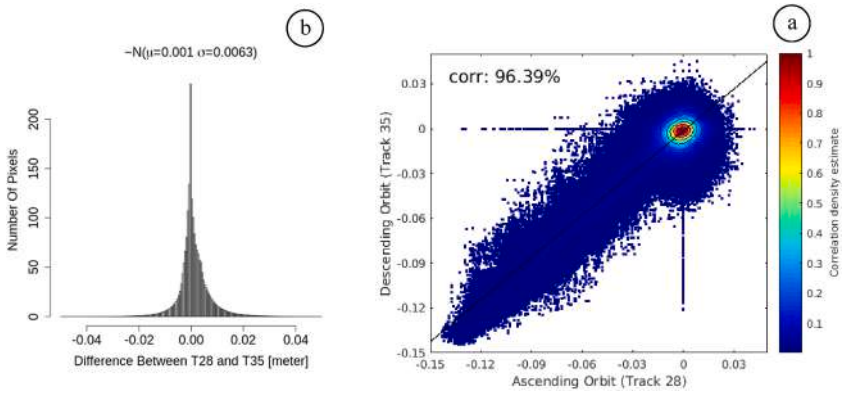

Fig. 10. Quantitative comparison between the estimated displacement rate in two ascending and descending orbits. a) Cross-correlation between measurement points. b) histogram of the analysis of the differences between the results.

Table 3
GNSS time series validation results.

SA1-Track vs. GPS	Correlation (%)	RMSE (cm)	Maximum diff. (cm)
Asc. Track 28	98.1 (P < 0.001)	(95% CI: 0.99, 1.14) 1.06	1.84
Des. Track 35	96.9 (P < 0.001)	(95% CI: 1.35, 1.58) 1.46	2.31

the subsidence of the GPS station (Fig. 11).

7. Discussion

According to the results of this study, subsidence in the southwest region of Tehran has been estimated to be over 20 cm annually in the vertical direction using the time series analysis of Sentinel-1A satellite radar images. This is while the subsidence of the southwest region of Tehran has always been significant due to its proximity to the city of Tehran and vital infrastructure. Therefore, in recent years, many researchers have monitored subsidence in this region, but the interesting point is the difference in subsidence monitoring results using interferometric radar time series analysis. The results also show a decrease in the subsidence rate in recent years. This decrease could be attributed to reduced water extraction, wells running dry, or increased precipitation rates in recent years. We performed a time series analysis of Sentinel-1A satellite radar data between 2015 and 2016 for the ascending orbit images to investigate this issue. The details of this dataset, including the network of interferometers and the coherence matrix between the interferograms, are shown in Fig. 12. As shown in Fig. 13, the estimated subsidence rate during this time is much higher than the subsidence calculated in recent years for the same orbit. That is, maximum LoS subsidence rates exceed −21 cm per year. Notably, there is an apparent trend that the annual subsidence rate has gradually decreased from January 2015 to January 2021. Specifically, the maximum subsidence rate for January 2020 to January 2021 has reduced to −18 cm per year. However, we may witness the local fluctuations in subsidence in some areas. The second point is that in the subsidence-affected area, several areas have subsidence rates that are significantly higher than other areas. Among these areas, the area near Tehran and residential areas has had more changes in the rate and pattern of subsidence and is gradually growing and expanding. The dynamics of subsidence in this area can seriously threaten residential areas and existing infrastructure in this region.

Given the importance of studying subsidence in the urban area of Tehran, the spatiotemporal distribution maps of subsidence signals from 2016 to the beginning of 2021 in this area are shown in Fig. 14. As can be seen, in addition to the gradual expansion of subsidence in this area, the cumulative displacement value is also very significant, reaching half a meter in some parts. This subsidence can be considered a severe threat to residential areas and some critical infrastructure in this area, such as Metro Lines, the Azadegan Expressway, the Tehran-Qom and Tehran-Tabriz railways, and the leading oil and gas transmission lines. Moreover, according to the latest subsidence zoning map in 2021, this area in urban areas has an extent of approximately 57 square kilometers (about 8% of the total Tehran city area). A comparison between the soil distribution map (Fig. 1) and the subsidence-affected areas in urban areas shows that subsidence has occurred more in areas where fine-grained soils occur, which are highly susceptible to subsidence. However, the expansion of subsidence in these areas can seriously threaten the infrastructure of this area and soon make this great metropolis face the world's biggest environmental challenge.

As we discussed earlier, the aquifer system in the Tehran plain receives recharge from several rivers. Among them, the Karaj and Kan rivers played the most significant role. However, the construction of a dam on the main rivers has made these rivers have a small contribution to feeding the aquifer of this plain. Instead, the Kan river over flooding season, the return flow from some parts of Tehran's urban sewage and industrial wastewater into local rivers and drainage channels have been the main surface water flows in groundwater recharge processes (Karamouz et al., 2004; Karimi et al., 2019). This change in recharge dynamics is essential to consider the relation between the subsidence and groundwater levels in the area. However, in this study without hydrological ground-based data to validate the results obtained, the subsidence data were compared with NDVI and NDMI indices and precipitation values

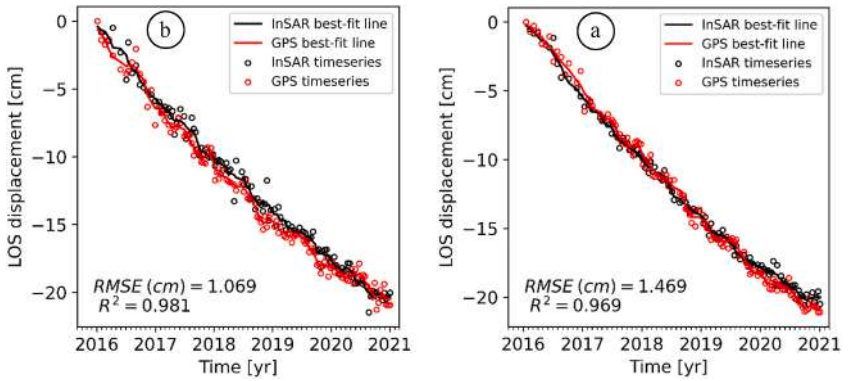

Fig. 11. A quantitative comparison between the estimated displacement time series in the ascending and descending orbits and the daily GPS observations in the subsidence area. a) Time series of the ascending orbit. b) Time series of the descending orbit.

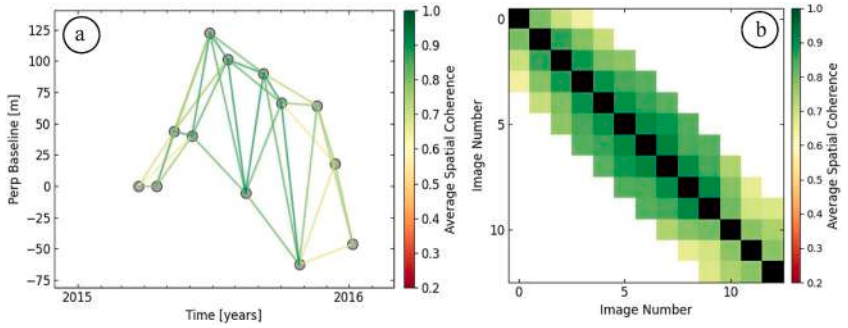

Fig. 12. a) Interferogram network created for the time interval between 2015 and 2016 for ascending orbit images, b) Coherence matrix between the interferograms.

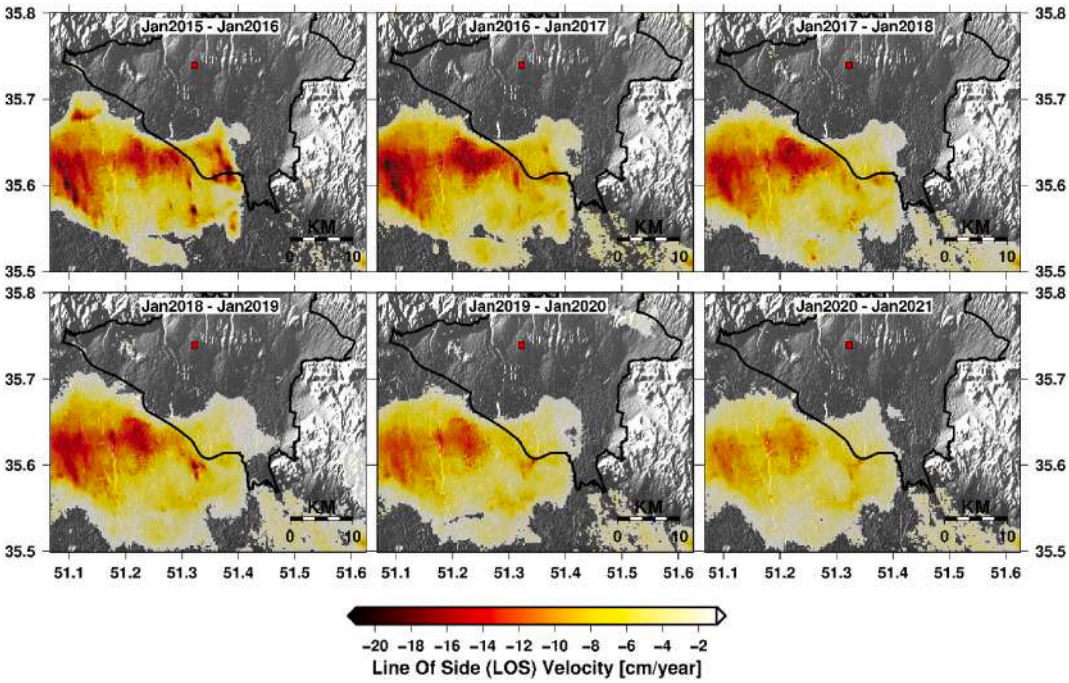

Fig. 13. Comparison between the mean annual velocity-field maps obtained from the Sentinel-1 ascending orbit images during the period of Jan 2015 to Jan 2016, Jan 2016 to Jan 2017, Jan 2017 to Jan 2018, Jan 2018 to Jan 2019, and Jan 2020 to Jan 2021. The local velocities higher than −1 cm/yr are masked out, and values lower than it are considered reliable measurements of subsidence.

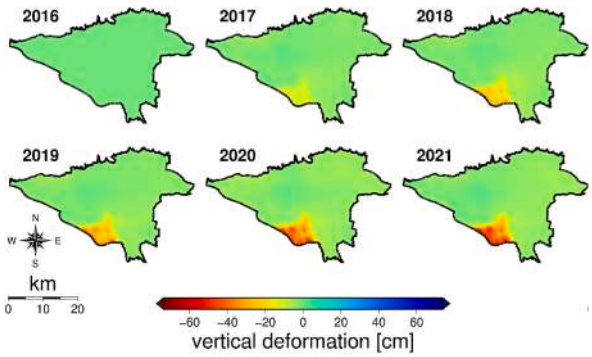

Fig. 14. Spatiotemporal pattern of cumulative subsidence from 2016 to the beginning of 2021 in the urban area of Tehran.

from 2015 to 2021 to assess their potential and mutual influence. The influence of groundwater depth and precipitation rates on both NDVI and NDMI parameters has been observed and analyzed in several studies (Phiri et al., 2018; Seeyan et al., 2014; Sewnet et al., 2016; Xu et al., 2023). Water-level changes are reflected in variations in vegetation coverage, plant diversity, and leaves and soil moisture content (indicated by higher NDVI and NDMI values, respectively). This can be correlated to shallow groundwater areas, where more water filtering into the soil supports agricultural increase. Conversely, areas with lower NDVI values might indicate less vegetation coverage and diversity, which can be associated with deeper groundwater levels and reduced soil moisture.

Fig. 15a and b illustrate the comparison between cumulative total precipitation (calculated by progressively summing daily precipitation over all the years under investigation) and smoothed NDVI and NDMI, respectively. Both graphs highlight significant changes in these indices in response to variations in precipitation rates. Overall, NDVI and NDMI values exhibit a positive correlation with increased rainfall, with lower values observed during periods of reduced rainfall (corresponding to low-slope segments in the cumulative total precipitation curve) and more pronounced increases immediately following heavy rainfall events (steep-slope segments), with a substantial increase in these values especially notable from 2018 onward.

In contrast, from 2015 to 2017, the precipitation trend remains relatively constant. This period is characterized by more significant subsidence, potentially attributed to water extraction rates for agriculture usage exceeding recharge rates and lower precipitation rates (as highlighted in other case studies, e.g. (Xu et al., 2023),).

In this scenario, we can hypothesize that higher NDVI, NDMI, and total precipitation from 2018 onwards may offset the rate of groundwater extraction in the area due to the groundwater recharge process and a rising water table resulting from an increase in

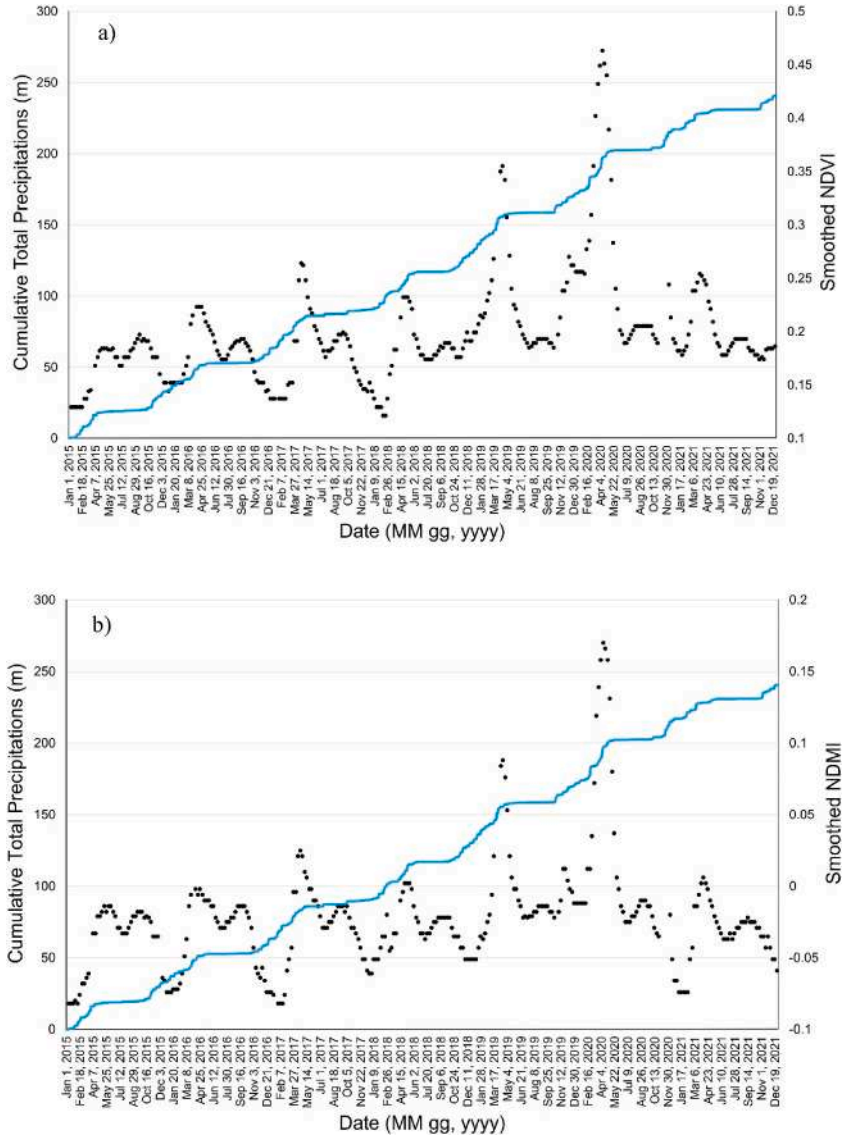

Fig. 15. Comparison between a) the Cumulative total precipitation and smoothed NDVI and b) the Cumulative total precipitation and smoothed NDMI.

precipitation rates, thereby causing a reduction in subsidence rates. To confirm what has been found in terms of the change in subsidence rates, the changes in NDVI indices for the two periods 2015–2017 and 2017–2021, respectively, are re-posted in Fig. 16. As can be seen, within the area's perimeter marked in yellow, where the highest subsidence rates were found, the highest rates of change in the NDVI index are also identified (red areas). This would confirm an increase in groundwater level over the period 2017–2021 and a consequent reduction in subsidence rates.

Short- and long-term plans are suggested to mitigate land subsidence and reduce potential risks. Short-term activities that need to be addressed include reducing the allowable pumping rate of groundwater wells, combating illegal drilling or exploitation of wells, developing modern irrigation methods such as drip irrigation, implementing watershed management plans, separating the drinking water system from non-potable and sanitary water use, reducing water losses in transmission networks, modifying the type of crops and orchards, particularly those with high water consumption, and assessing the risk of land subsidence on structures and infrastructure to reinforce them. In the long-term, plans include modifying the management mindset (small or large-scale) in environmental decision-making based on the ecological reality of the region, improving education and lifestyle to understand the laws governing nature instead of relying on engineering and structural capabilities, designing the layout and development axis based on ecological and potential advantages rather than short-term needs and interests, and ultimately, striving to raise children and generations who respect the environment.

As a limitation of the current study, the unavailability of underground water levels data and changes in the water level of underground aquifers data in the region. The lack of such data prevents a comprehensive analysis of land subsidence over time and hinders the ability to simulate subsidence probabilities in real-time. Therefore, if the aforementioned data set is available, it is recommended that these datasets be used as a key variable in modeling the spatiotemporal land subsidence with the help of radar observations and machine learning models in future research. Furthermore, this study investigated land subsidence from 2015 to the beginning of 2021. The processing of more recent SAR images (i.e., 2022 to 2024) can increase the accuracy of the results and evaluate the assumption of a decrease in the subsidence rate in recent years. Moreover, to study non-linear anomalies of displacement (e.g., some sort of subsidence seasonality), exploring non-linear models or spatially classifying regions to consider different displacement patterns for each region would be advisable.

8. Conclusion and perspectives

This study analyzes the time series of Sentinel-1A images collected between 2016 and the end of 2020 over the Tehran Plain to investigate the spatiotemporal of land subsidence turned in collaboration by the Landsat 8 OLI/TIRS sensors. The following conclusions can be summarized based on the results obtained.

- A review of the history of studies shows that due to the importance of Tehran city, many researchers have investigated the subsidence in this area; however, there are differences in the maximum rate of subsidence reported in these studies.
- The maximum subsidence rate over the Tehran plain is approximately 20 cm per year from 2016 to the end of 2020.
- Subsidence tongues are being extended from the south and southwest into Tehran city, mainly including fine-grained soil areas.
- The maximum absolute horizontal displacement rate is around 8 cm per year in the east-west direction.
- Neglecting the horizontal component, the maximum error in calculating the vertical displacement rate is 7 and 6.1 cm per year for the ascending and descending orbits, respectively.
- Significant subsidence continuously occurs and expands in this plain. However, the rate of subsidence has slowly decreased in recent years. This could be attributed to the balancing effect on the groundwater extraction rate in the area. This effect results from the groundwater recharge process and the rising water table, a consequence of increased precipitation rates starting in 2018. This is also evident from the analysis of variations in NDVI and NDMI indices.

Based on these results, increasing our understanding of these complex relationships of subsidence with the other factors will lead to more effective solutions for solving this problem. Future studies in this direction and towards understanding the intelligence of land subsidence in the area, especially in urban areas, can assist higher-level authorities in improving planning to strengthen the proper management of water resources, prevent adverse decisions, and assess the associated risk. Also, there is potential for future research to

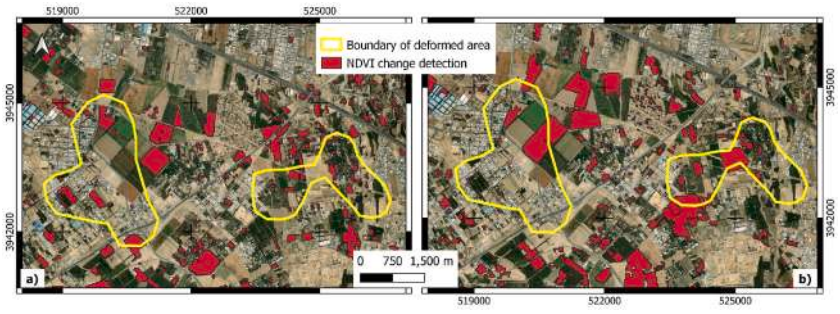

Fig. 16. NDVI change detection: a) 2015–2017; b) 2017–2021. Yellow boundaries identified areas affected by higher subsidence rates. (For interpretation of the references to color in this figure legend, the reader is referred to the Web version of this article.)

focus on developing a subsidence risk map based on subsidence gradients and exposure and vulnerability of the elements at risk (e.g., population density, infrastructure, housing), which is the key factor to the assessment of the level of risk posed by land subsidence and urban development plans.

Funding

Open access funding provided by the University of Napoli' Federico II.'

Additional information

Correspondence and requests for materials should be addressed to M.A.Kh.

CRediT authorship contribution statement

Sasan Babaee: Writing – original draft, Visualization, Validation, Software, Formal analysis, Conceptualization. **Mohammad Amin Khalili:** Writing – original draft, Visualization, Software, Methodology, Investigation, Conceptualization. **Rita Chirico:** Visualization, Validation, Resources, Investigation. **Anna Sorrentino:** Visualization, Resources, Investigation. **Diego Di Martire:** Writing – review & editing, Supervision, Resources, Project administration, Formal analysis.

Declaration of competing interest

The authors declare the following financial interests/personal relationships which may be considered as potential competing interests:

Mohammad Amin Khalili reports article publishing charges was provided by University of Naples Federico II. If there are other authors, they declare that they have no known competing financial interests or personal relationships that could have appeared to influence the work reported in this paper.

Data availability

Data will be made available on request.

Acknowledgment

This study was carried out within the RETURN Extended Partnership and received funding from the European Union Next-GenerationEU (National Recovery and Resilience Plan – NRRP, Mission 4, Component 2, Investment 1.3 – D.D. 1243 August 2, 2022, PE0000005). The authors of this study sincerely thank the European Space Agency (ESA) for providing free Sentinel-1A radar SAR images and the spatial information technology organization in Tehran for providing GPS time series data.

References

Ahadnejad, V., Hirt, A.M., Alizadeh, H., 2016. Geological constraints on sustainable urban growth and management of the metropolis of Tehran, Iran. Geol. Soc. Am. Spec. Pap. 520, 273–286.

Ajourlou, P., Esfahany, S.S., Safari, A., 2019. A new strategy for phase unwrapping in Insar time series over areas with high deformation rate: case study on the Southern Tehran subsidence. Int. Arch. Photogramm. Remote Sens. Spat. Inf. Sci. 42, 35–40.

Alipour, S., Motgah, M., Sharifi, M., Walter, T.R., 2008. InSAR time series investigation of land subsidence due to groundwater overexploitation in Tehran, Iran. In: Presented at the 2008 Second Workshop on Use of Remote Sensing Techniques for Monitoring Volcanoes and Seismogenic Areas. IEEE, pp. 1–5.

Aljammaz, A., Sultan, M., Izadi, M., Abotalib, A.Z., Elhebiry, M.S., Emil, M.K., Abdelmohsen, K., Saleh, M., Becker, R., 2021. Land subsidence induced by rapid urbanization in arid environments: a remote sensing-based investigation. Rem. Sens. 13, 1109. https://doi.org/10.3390/rs13061109.

Amighpey, M., Arabi, S., Talebi, A., Djamour, Y., 2006. Elevation changes of the precise leveling tracks in the Iran leveling network. Scientific Report Published in National Cartographic Center (NCC) of Iran.

Amin Khalili, M., Di Muro, C., Guerriero, L., Ramondini, M., Calcaterra, D., Di Martire, D., 2024. Evaluating the effectiveness of deep learning algorithms and InSAR data in early warning systems for landslide risk mitigation, 107–113. https://doi.org/10.18485/resylab.2024.6.ch13.

Arabi, S., Montazerian, A.R., Maleki, E., Talebi, A., 2005. Study of land subsidence in southwest of Tehran plain basin. J. Natl. Cartogr. Cent. NCC Iran 16 (69), 14–28.

Azadnejad, S., Maghsoudi, Y., Perissin, D., 2019. Investigating the effect of the physical scattering mechanism of the dual-polarization sentinel-1 data on the temporal coherence optimization results. Int. J. Rem. Sens. 40, 7033–7047.

Babaee, S., Hossainali, M.M., Esfahany, S.S., 2022. Assessment of noise in InSAR timeseries using least squares variance component estimation. Ann. Geophys. 65.

Bagheri-Gavkosh, M., Hosseini, S.M., Ataie-Ashtiani, B., Sohani, Y., Ebrahimian, H., Morovat, F., Ashrafi, S., 2021. Land subsidence: a global challenge. Sci. Total Environ. 778, 146193 https://doi.org/10.1016/j.scitotenv.2021.146193.

Baniani, S.R., Chang, L., Maghsoudi, Y., 2021. Mapping and analyzing land subsidence for Tehran using Sentinel-1 SAR and GPS and geological data (No. EGU21-295). Copernicus Meetings. https://doi.org/10.5194/egusphere-egu21-295. Presented at the EGU21.

Bausilio, G., Khalili, M.A., Virelli, M., Di Martire, D., 2024. Italian COSMO-SkyMed atlas: R-Index and the percentage of measurability of movement. GIScience Remote Sens. 61, 2312705 https://doi.org/10.1080/15481603.2024.2312705.

Berardino, P., Fornaro, G., Lanari, R., Sansosti, E., 2002. A new algorithm for surface deformation monitoring based on small baseline differential SAR interferograms. IEEE Trans. Geosci. Rem. Sens. 40, 2375–2383. https://doi.org/10.1109/TGRS.2002.803792.

Castellazzi, P., Arroyo-Domínguez, N., Martel, R., Calderhead, A.I., Normand, J.C.L., Gárfias, J., Rivera, A., 2016. Land subsidence in major cities of Central Mexico: interpreting InSAR-derived land subsidence mapping with hydrogeological data. Int. J. Appl. Earth Obs. Geoinformation 47, 102–111. https://doi.org/10.1016/j.jag.2015.12.002.

Coda, S., Tessitore, S., Di Martire, D., Calcaterra, D., De Vita, P., Allocca, V., 2019. Coupled ground uplift and groundwater rebound in the metropolitan city of Naples (southern Italy). J. Hydrol. 569, 470–482. https://doi.org/10.1016/j.jhydrol.2018.11.074.

De Zan, F., Guarnieri, A.M., 2006. TOPSAR: terrain observation by progressive scans. IEEE Trans. Geosci. Rem. Sens. 44, 2352–2360.

Dehghani, M., Zoej, M.J.V., Hooper, A., Hanssen, R.F., Entezam, I., Saatchi, S., 2013. Hybrid conventional and persistent scatterer SAR interferometry for land subsidence monitoring in the Tehran Basin, Iran. ISPRS J. Photogrammetry Remote Sens. 79, 157–170.
Djamour, Y., Nankali, H., Sedighi, M., Sadeghi, F., Rahimi, Z., Tavakoli, F., Mousavi, Z., Khorrami, F., Aghamohammadi, A., Hosseini, S., 2007. First results inferred from the new Iranian permanent GPS network for geodynamics (IPGN). Presented at the Geophysical Research Abstracts, 04910.
Efron, B., Tibshirani, R., 1985. The bootstrap method for assessing statistical accuracy. Behaviormetrika 12, 1–35.
Engalenc, M., 1968. Contribution à l'étude géologique, géomorphologique et hydrogéologique de la région de Téhéran (Iran). Éditeur Non Identifié.
Esmaeili, M., Motagh, M., 2016. Improved Persistent Scatterer analysis using Amplitude Dispersion Index optimization of dual polarimetry data. ISPRS J. Photogrammetry Remote Sens. 117, 108–114.
Esmaeili, M., Motagh, M., Hooper, A., 2017. Application of dual-polarimetry SAR images in multitemporal InSAR processing. Geosci. Rem. Sens. Lett. IEEE 14, 1489–1493.
Fattahi, H., Agram, P., Simons, M., 2016. A network-based enhanced spectral diversity approach for TOPS time-series analysis. IEEE Trans. Geosci. Rem. Sens. 55, 777–786.
Ferretti, A., Colombo, D., Fumagalli, A., Novali, F., Rucci, A., 2015. InSAR data for monitoring land subsidence: time to think big. Proc. IAHS 372, 331–334. https://doi.org/10.5194/piahs-372-331-2015.
Foroughnia, F., Nemati, S., Maghsoudi, Y., Perissin, D., 2019. An iterative PS-InSAR method for the analysis of large spatio-temporal baseline data stacks for land subsidence estimation. Int. J. Appl. Earth Obs. Geoinformation 74, 248–258.
Gourmelen, N., Peyret, M., Fritz, J., Cherry, J., 2003. Ground surface deformation around tehran due to groundwater recharge: InSAR monitoring. Presented at the Applications of SAR Polarimetry and Polarimetric Interferometry.
Haghighi, M.H., Motagh, M., 2019. Ground surface response to continuous compaction of aquifer system in Tehran, Iran: results from a long-term multi-sensor InSAR analysis. Remote Sens. Environ. 221, 534–550.
Haghshenas Haghighi, M., Motagh, M., Esmaeili, M., 2013. Continuous compaction of aquifer system in Tehran, Iran, as evidenced by C-band, L-band and X-band radar measurements. Presented at the 5th TerraSAR-X/4th TanDEM-X Science Team Meeting (Oberpfaffenhofen, Germany 2013).
Hanssen, R.F., 2001. Radar Interferometry: Data Interpretation and Error Analysis. Springer Science & Business Media.
Herrera, G., Tomás, R., Monells, D., Centolanza, G., Mallorquí, J.J., Vicente, F., Navarro, V.D., Lopez-Sanchez, J.M., Sanabria, M., Cano, M., Mulas, J., 2010. Analysis of subsidence using TerraSAR-X data: murcia case study. Eng. Geol. 116, 284–295. https://doi.org/10.1016/j.enggeo.2010.09.010.
Jeanne, P., Farr, T.G., Rutqvist, J., Vasco, D.W., 2019. Role of agricultural activity on land subsidence in the San Joaquin Valley, California. J. Hydrol. 569, 462–469. https://doi.org/10.1016/j.jhydrol.2018.11.077.
Karamouz, M., Kerachian, R., Zahraie, B., 2004. Monthly water resources and irrigation planning: case study of conjunctive use of surface and groundwater resources. J. Irrigat. Drain. Eng. 130, 391–402. https://doi.org/10.1061/(ASCE)0733-9437(2004)130:5391.
Karimi, L., Motagh, M., Entezam, I., 2019. Modeling groundwater level fluctuations in Tehran aquifer: results from a 3D unconfined aquifer model. Groundw. Sustain. Dev. 8, 439–449. https://doi.org/10.1016/j.gsd.2019.01.003.
Khalili, M.A., Bausilio, G., Di Muro, C., Zampelli, S.P., Di Martire, D., 2023. Investigating Gravitational Slope Deformations with COSMO-SkyMed-Based Differential Interferometry: A Case Study of San Marco dei Cavoti. Appl. Sci. 13, 6291. https://doi.org/10.3390/app13106291.
Landsat Collection 2 U.S. Analysis Ready Data (USGS Numbered Series No. 2023–3015), 2023. Landsat Collection 2 U.S. Analysis Ready Data, Fact Sheet. U.S. Geological Survey, Reston, VA. https://doi.org/10.3133/fs20233015.
Li, S., Xu, L., Jing, Y., Yin, H., Li, X., Guan, X., 2021. High-quality vegetation index product generation: a review of NDVI time series reconstruction techniques. Int. J. Appl. Earth Obs. Geoinformation 105, 102640. https://doi.org/10.1016/j.jag.2021.102640.
Liu, Z., Mei, G., Sun, Y., Xu, N., 2021. Investigating mining-induced surface subsidence and potential damages based on SBAS-InSAR monitoring and GIS techniques: a case study. Environ. Earth Sci. 80, 817. https://doi.org/10.1007/s12665-021-09726-z.
Maghrebi, M., Noori, R., Mehr, A.D., Lak, R., Darougheh, F., Razmgir, R., Farnoush, H., Taherpour, H., Moghaddam, S.M.R.A., Araghi, A., Kløve, B., 2023. Spatiotemporal changes in Iranian rivers' discharge. Elem. Sci. Anthr. 11, 00002. https://doi.org/10.1525/elementa.2022.00002.
Maghsoudi, Y., Amani, R., Ahmadi, H., 2021. A study of land subsidence in west of Tehran using Sentinel-1 data and permanent scatterer interferometric technique. Arabian J. Geosci. 14, 1–10.
Mahmoudpour, M., Khamehchiyan, M., Nikudel, M., Gassemi, M., 2013. Characterization of regional land subsidence induced by groundwater withdrawals in Tehran, Iran. Geopersia 3, 49–62.
Mahmoudpour, M., Khamehchiyan, M., Nikudel, M.R., Ghassemi, M.R., 2016. Numerical simulation and prediction of regional land subsidence caused by groundwater exploitation in the southwest plain of Tehran, Iran. Eng. Geol. 201, 6–28.
Masson, F., Sedighi, M., Hinderer, J., Bayer, R., Nilforoushan, F., Luck, J.-M., Vernant, P., Chery, J., 2002. Present-day surface deformation and vertical motion in the central Alborz (Iran) from GPS and absolute gravity measurements. Presented at the EGS General Assembly Conference Abstracts, p. 455.
Motagh, M., Shamshiri, R., Haghighi, M.H., Wetzel, H.-U., Akbari, B., Nahavandchi, H., Roessner, S., Arabi, S., 2017. Quantifying groundwater exploitation induced subsidence in the Rafsanjan plain, southeastern Iran, using InSAR time-series and in situ measurements. Eng. Geol. 218, 134–151.
Motagh, M., Walter, T.R., Sharifi, M.A., Fielding, E., Schenk, A., Anderssohn, J., Zschau, J., 2008. Land subsidence in Iran caused by widespread water reservoir overexploitation. Geophys. Res. Lett. 35.
Muñoz-Sabater, J., Dutra, E., Agustí-Panareda, A., Albergel, C., Arduini, G., Balsamo, G., Boussetta, S., Choulga, M., Harrigan, S., Hersbach, H., Martens, B., Miralles, D.G., Piles, M., Rodríguez-Fernández, N.J., Zsoter, E., Buontempo, C., Thépaut, J.-N., 2021. ERA5-Land: a state-of-the-art global reanalysis dataset for land applications. Earth Syst. Sci. Data 13, 4349–4383. https://doi.org/10.5194/essd-13-4349-2021.
Papi, R., Attarchi, s., Soleimani, M., 2020. Analysing time series of land subsidence in the west of tehran province (shahriar plain) and its relation to groundwater discharge by InSAR technique. Geogr. Environ. Sustain. 10, 109–128. https://doi.org/10.22126/ges.2020.4933.2182.
Park, H., Kwon, S., Hadi, S., 2016. Land subsidence survey and policy development in pantai mutiara, Jakarta bay, Indonesia. J. Coast Res. (1), 1447–1451. https://doi.org/10.2112/SI75-300.
Phiri, M., Shiferaw, Y.A., Tesfamichael, S.G., 2018. Modelling the relationship between groundwater depth and NDVI using time series regression with Distributed Lag M. South Afr. J. Geom. 7, 147–163.
Pirouzi, A., Eslami, A., 2017. Ground subsidence in plains around Tehran: site survey, records compilation and analysis. Int. J. Geo-Eng. 8, 1–21.
Rosen, P.A., Gurrola, E.M., Sacco, G., Zebker, H.A., 2011. InSAR Scientific Computing Environment - the Home Stretch 2011. IN42A-02.
Samieie-Esfahany, S., Hanssen, R., van Thienen-Visser, K., Muntendam-Bos, A., 2009. On the effect of horizontal deformation on InSAR subsidence estimates. In: Presented at the Proceedings of the Fringe 2009 Workshop. Frascati, Italy.
Santos, S.M. dos, Cabral, J.J., Pontes Filho, I.D., 2012. Monitoring of soil subsidence in urban and coastal areas due to groundwater overexploitation using GPS. Nat. Hazards 64, 421–439. https://doi.org/10.1007/s11069-012-0247-9.
Schenk, A., 2006. Interpreting Surface Displacement in Tehran/Iran Region Observed by Differential Synthetic Aperture Radar Interferometry (DINSAR). MSc Thesis. Tech. Univ., Berlin, Berlin, Germany.
Seeyan, S., Merkel, B., Abo, R., 2014. Investigation of the relationship between groundwater level fluctuation and vegetation cover by using NDVI for shaqlawa basin, kurdistan region – Iraq. J. Geogr. Geol. 6, p187. https://doi.org/10.5539/jgg.v6n3p187.
Sewnet, D., Naqvi, H.R., Athick, A., 2016. Zonation of potential groundwater and its spatial correlation with indices and boreholes: western region of blue nile basin, Ethiopia. J. Remote Sens. GIS 7, 22–34.
Shemshaki, A., Blourchi, M.J., Ansari, F., 2005. Study of land subsidence in the plain of Tehran Shhriar. Eng. Geol. Environ. Manag. Group Geol. Surv. Iran Minist. Ind. Mines 84–06.
Shirzad, T., Hossein Shomali, Z., 2014. Shallow crustal structures of the Tehran basin in Iran resolved by ambient noise tomography. Geophys. J. Int. 196, 1162–1176. https://doi.org/10.1093/gji/ggt449.

Taheri Dehkordi, A., Valadan Zoej, M.J., Ghasemi, H., Ghaderpour, E., Hassan, Q.K., 2022. A new clustering method to generate training samples for supervised monitoring of long-term water surface dynamics using Landsat data through Google Earth engine. Sustainability 14, 8046. https://doi.org/10.3390/su14138046.

Tarighat, F., Foroughnia, F., Perissin, D., 2021. Monitoring of power towers' movement using persistent scatterer SAR interferometry in south west of tehran. Rem. Sens. 13, 407.

Tzampoglou, P., Ilia, I., Karalis, K., Tsangaratos, P., Zhao, X., Chen, W., 2023. Selected worldwide cases of land subsidence due to groundwater withdrawal. Water 15, 1094. https://doi.org/10.3390/w15061094.

Valente, E., Allocca, V., Riccardi, U., Camanni, G., Di Martire, D., 2021. Studying a subsiding urbanized area from a multidisciplinary perspective: the inner sector of the sarno plain (southern apennines, Italy). Rem. Sens. 13, 3323. https://doi.org/10.3390/rs13163323.

Vermote, E., Justice, C., Claverie, M., Franch, B., 2016. Preliminary analysis of the performance of the Landsat 8/OLI land surface reflectance product. Remote Sens. Environ., Landsat 8 Science Results 185, 46–56. https://doi.org/10.1016/j.rse.2016.04.008.

Vernant, P., Nilforoushan, F., Chéry, J., Bayer, R., Djamour, Y., Masson, F., Nankali, H., Ritz, J.-F., Sedighi, M., Tavakoli, F., 2004. Deciphering oblique shortening of central Alborz in Iran using geodetic data. Earth Planet Sci. Lett. 223, 177–185. https://doi.org/10.1016/j.epsl.2004.04.017.

Wall, M.E., Rechtsteiner, A., Rocha, L.M., 2003. Singular value decomposition and principal component analysis. In: Berrar, D.P., Dubitzky, W., Granzow, M. (Eds.), A Practical Approach to Microarray Data Analysis. Kluwer Academic Publishers, Boston, pp. 91–109. https://doi.org/10.1007/0-306-47815-3_5.

Wasowski, J., Bovenga, F., 2014. Investigating landslides and unstable slopes with satellite Multi Temporal Interferometry: current issues and future perspectives. Eng. Geol. 174, 103–138. https://doi.org/10.1016/j.enggeo.2014.03.003.

Xu, X., Zhou, C., Gong, H., Chen, B., Wang, L., 2023. Monitoring and analysis of land subsidence in cangzhou based on small baseline subsets interferometric point target analysis technology. Land 12, 2114. https://doi.org/10.3390/land12122114.

Yunjun, Z., Fattahi, H., Amelung, F., 2019. Small baseline InSAR time series analysis: unwrapping error correction and noise reduction. Comput. Geosci. 133, 104331.